

# Politecnico di Torino

Master's Degree in Mechatronic Engineering



Master's Degree Thesis

## Modelling and Simulation of Faulty Electromechanical Actuators

**Supervisor**

Prof. Massimo Sorli

**Co-Supervisor**

Ing. Andrea De Martin

**Candidate**

Rosita Berterame



# Index

<i>Figures Index</i> .....	5
<i>Tables Index</i> .....	8
CHAPTER I: INTRODUCTION.....	11
CHAPTER II: PROGNOSTIC AND HEALTH MANAGEMENT.....	13
2.1 INTRODUCTION TO PHM.....	13
2.1.1 <i>Fault Diagnosis</i> .....	18
2.1.2 <i>Fault Prognosis</i> .....	20
2.1.3 <i>Performance Metrics</i> .....	25
2.2 PREDICTION CONFIDENCE METRICS.....	28
2.3 ADVANTAGES OF USING PHM.....	30
CHAPTER III: FAULT TOLERANT CONTROL.....	32
3.1 INTRODUCTION OF RECONFIGURABLE CONTROL.....	32
3.2 MODEL PREDICTIVE CONTROL.....	34
3.3 MPC STRATEGY.....	35
3.3.1 <i>MPC Controller Model</i> .....	39
3.3.2 <i>MPC Implementation</i> .....	40
CHAPTER IV: TEST BENCH COMPONENTS.....	43
4.1 ELECTROMECHANICAL ACTUATORS.....	43
4.2 COMPONENTS DESCRIPTION.....	45
4.2.1 <i>EMA Configuration and Working Principle</i> .....	47
4.2.2 <i>Mechanical Transmission</i> .....	54
CHAPTER V: VIBRATION SIGNALS AS FUNCTION OF STATIC AIRGAP ECCENTRICITY IN EM.....	55
5.1 ECCENTRICITY IN ELECTRIC MOTORS.....	56

## Index

---

5.2 DETECTION OF ROTOR ECCENTRICITY IN EM.....	60
CHAPTER VI: LINEAR MODEL OF THE EMA.....	63
6.1 EMA MODEL.....	64
6.1.1 <i>Electric model</i> .....	64
6.1.2 <i>Mechanical transmission</i> .....	65
6.1.3 <i>Equilibrium rotation equation of motor shaft</i> .....	66
6.2 CONTROL MODELLING.....	66
6.3 SIMULINK MODEL OF THE SERVOSYSTEM.....	70
6.4 AIRGAP-LENGTH VARIATION BLOCK MODEL.....	75
CHAPTER VII: SIMULATION ACTIVITIES SETTING.....	77
7.1 PRELIMINARY SYSTEM ANALYSIS.....	77
7.2 MOTOR CURRENT SIGNATURE ANALYSIS (MCSA) FOR FAULT DETECTION.....	81
CHAPTER VIII: SE FAULT SIMULATION AND DIAGNOSIS THROUGH SIDEBANDS IN FFT ANALYSIS.....	83
8.1 DIAGNOSIS AT NO-LOAD.....	83
8.2 DIAGNOSIS AT DIFFERENT LOADS.....	86
8.2.1 <i>Diagnosis at <math>F = 200 N</math></i> .....	86
8.2.2 <i>Diagnosis with <math>F = 500 N</math></i> .....	88
8.3 RESULT ANALYSIS.....	89
8.4 FEATURE EXTRACTION.....	95
CHAPTER IX: CONCLUSIONS AND FURTHER STUDIES.....	96
APPENDIX.....	98
A - TOTAL INERTIAL MODEL ON THE MOTOR SHAFT.....	98
B - SIDEBAND FREQUENCIES PEAKS MAGNITUDE.....	100
BIBLIOGRAPHY.....	104

# Figures Index

Fig. 1 - An integrated approach to CBM/PHM design.....	15
Fig. 2 – The CBM/PHM cycle.....	16
Fig. 3 – General FDI structure.....	19
Fig. 4 – Alarm bounds on measured sensor signals.....	20
Fig. 5 – Fault propagation.....	21
Fig. 6 – Physics-based modelling approach.....	22
Fig. 7 – Manufacturing variability and mission history effects.....	23
Fig. 8 – (a) The RUL pdf and the Just-In-Time removal-from-service point; (b) the RUL pdf as time-varying conditional pdf.....	24
Fig. 9 – Time evolution of the RUL pdf.....	25
Fig. 10 – Predicted and actual failure times and the associated accuracy.....	27
Fig. 12 – Precision dependency on prediction confidence bounds, R: (a) higher precision output and (b) lower precision output.....	28
Fig. 13 – Possibility density function for confidence bounds.....	29
Fig. 14 – Time evolution of the distribution at the hazard line.....	30
Fig. 15 – The Prognostic Framework.....	31
Fig. 16 – State transition diagram for low level reconfigurable control.....	33
Fig. 17 – MPC controller state at the k-th sampling instant.....	37
Fig. 18 – Model Predictive Controller structure.....	38
Fig. 19 – Block diagram of the MPC with plant and signals.....	41
Fig. 20 – Typical architecture of an Electromechanical actuator for flight controls....	45

## Figure Index

---

Fig. 21 – Ac motor. Three-phase power supply for a two-poles synchronous motor at $0^\circ, 30^\circ, 60^\circ, 90^\circ$ .....	49
Fig. 22 –Field Oriented Control coordinates transformation.....	50
Fig. 23 – Field Oriented Control block diagram.....	52
Fig. 24 – Resolver working principle.....	53
Fig. 25 – Rotor eccentricity representation.....	59
Fig. 26 - Representation of static (a), dynamic (b) and mixed (c) eccentricities, for revolving rotor (black arrow).....	59
Fig. 27 – High fidelity block diagram of EMA model.....	64
Fig. 28 – Position Control Loop block.....	67
Fig. 29 – Speed Control Loop block.....	67
Fig. 30 – Current Control Loop using FOC.....	68
Fig. 31 – Current Decoupled Control Loop block.....	69
Fig. 32 - The frequency response of a Proportional-Integrative contribution.....	70
Fig. 33 – Simulink physical model.....	72
Fig. 34 – Physical block model with the control loops.....	73
Fig. 35. – Airgap variation block.....	76
Fig. 36 – Back-emf of phase a signals plot in no-load condition at nominal speed $\omega_r$ .....	78
Fig. 37 – Current $i_a$ signals plot in no-load condition at nominal speed $\omega_r$ .....	79
Fig. 38 – Torque signals plot in no-load condition at nominal speed $\omega_r$ .....	79
Fig. 39 – Back-emf $e_a$ signals plot with $0.5F_{ext}$ and $0.3\omega_r$ .....	80
Fig. 40 – Current $i_a$ signals plot with $0.5F_{ext}$ and $0.3\omega_r$ .....	80
Fig. 41 – Torque signals plot with $0.5F_{ext}$ and $0.3\omega_r$ .....	81
Fig. 42 – FFT response of the current signal at $0.3\omega_r$ in no-load condition.....	84

## Figure Index

---

Fig. 43 – FFT response of the current signal at $0.5\omega_r$ in no-load condition.....	85
Fig. 44 – FFT response of the current signal at $\omega_r$ in no-load condition.....	85
Fig. 45 – FFT response of the current signal at $0.3\omega_r$ with $F = 200\text{ N}$ .....	87
Fig. 46 – FFT response of the current signal at $0.5\omega_r$ with $F = 200\text{ N}$ .....	87
Fig. 47 – FFT response of the current signal at $\omega_r$ with $F = 200\text{ N}$ .....	88
Fig. 48 – FFT response of the current signal at $0.3\omega_r$ with $F = 500\text{ N}$ .....	88
Fig. 49 – FFT response of the current signal at $0.5\omega_r$ with $F = 500\text{ N}$ .....	89
Fig. 50 – FFT response of the current signal at $\omega_r$ with $F = 500\text{ N}$ .....	89
Fig. 51 – Sidebands variation of current $i_a$ with SE at $\omega_r$ : (a) with no-load; (b) with $F = 200\text{ N}$ ; (c) with $F = 500\text{ N}$ .....	91
Fig. 52 - Sidebands variation of current $i_a$ with SE at $0.5\omega_r$ : (a) with no-load; (b) with $F = 200\text{ N}$ ; (c) with $F = 500\text{ N}$ .....	93
Fig. 53 - Sidebands variation of current $i_a$ with SE at $0.3\omega_r$ : (a) with no-load; (b) with $F = 200\text{ N}$ ; (c) with $F = 500\text{ N}$ .....	94

# Tables Index

Tab.1 – LEMC 2105 general parameters.....	30
Tab. 2 – Electric Motor rated data.....	30
Tab. 3 – Rated data of the satellite roller screw SKF actuator.....	38
Tab. 4 – System working conditions.....	63
Tab. 5 – Magnitude [A] of sideband components at $0.3\omega_r$ with $F_{ext} = 0 N$ .....	88
Tab. 6 – Magnitude [A] of sideband components at $0.5\omega_r$ with $F_{ext} = 0 N$ .....	88
Tab. 7 – Magnitude [A] of sideband components at $\omega_r$ with $F_{ext} = 0 N$ .....	88
Tab. 8 – Magnitude [A] of sideband components at $0.3\omega_r$ with $F_{ext} = 200 N$ .....	89
Tab. 9 – Magnitude [A] of sideband components at $0.5\omega_r$ with $F_{ext} = 200 N$ .....	89
Tab. 10 – Magnitude [A] of sideband components at $\omega_r$ with $F_{ext} = 200 N$ .....	89
Tab. 11 – Magnitude [A] of sideband components at $0.3\omega_r$ with $F_{ext} = 500 N$ .....	90
Tab. 12 – Magnitude [A] of sideband components at $0.5\omega_r$ with $F_{ext} = 500 N$ .....	90
Tab. 13 – Magnitude [A] of sideband components at $\omega_r$ with $F_{ext} = 500 N$ .....	90





# Chapter I

## Introduction

Over the last few decades, the *Prognostics and Health Management* (PHM) technique has found more and more space in many engineering and industrial sectors. This technique aims to forecast accurately the fault/failure occurrence or the Remaining Useful Life of critical components and to quickly detect and isolate the root causes of failure. The big stages that compose this technique are the *diagnosis* and the *prognosis*. The first deals with the detection of faults or anomaly conditions, the isolation of the faulty components detected in a system or process and the assessment of their possible effects on the system's health. In this regard, the indices related to particular failures are extracted; they determine through the probability density function the performances of the failing system. The prognosis, instead, is the ability to forecast accurately and precisely the Remaining Useful Life (RUL) of a failing component of the system. As shown in many studies [1-2], prognostics is used in other technological fields and could be very useful to condition based maintenance, since it reduces both costs and inspection time. Modern technological systems relied on sophisticated control systems for prognostic purposes have been developed over the years to meet increased performance and safety requirements. One of these fault-tolerant and reconfigurable control strategies proposed here is the MPC controller, but its practical application is not investigated in this work.

This Thesis aims to verify the reliability of the PHM diagnosis implemented on an electromechanical actuator (EMA), which uses a three-phase permanent magnet synchronous motor (PMSM). The obtained model of the EMA replicates one of the most common electric motors fault, that is, the rotor static eccentricity. In the reality, this phenomenon could be due to assembly error or to progressive wear of rotor bearings. For diagnostic purposes, the Fourier Fast Transform (FFT) is used as fault identification

techniques able to reveal the presence of rotor eccentricity thanks to the current frequency spectrum. The pursued study confirmed the reliability of the FFT as diagnosis technique, revealing a dependency of the frequency sidebands present in the current frequency spectrum on the static eccentricity ratio and on the rotor speed. This has set the basis for extracting a fault feature that unequivocally describes the system behavior in the presence of this incipient fault.

The rest of the work is developed as follows. In Chapter II a detailed description of the PHM technique is given, sorting through all the phases, which characterize it. In Chapter III the innovative fault tolerant control methodology, namely the Model Predictive Control technique, is presented, highlighting its functionalities and suggesting a possible implementation with systems such as the studied EMA. In Chapter IV the electromechanical actuator present in the flight-control test bench and its working principle are described. In Chapter V the static eccentricity fault for an electrical motor is outlined. Here can be found also a presentation of the Fast Fourier Transform analysis as diagnostic approach. In Chapter VI the MATLAB/Simulink model used to characterize the behaviour the whole servosystem during the simulation investigations is described.

In Chapter VII the preliminary tests on the system for the fault identification are reported, comparing the system response under healthy and faulty condition. In Chapter VIII the FFT analysis is exploited, in order to verify the presence of the rotor static eccentricity thanks to the sidebands occurred in the current frequency response. A first hypothesis of the fault feature is also proposed. Finally, in Chapter IX the conclusions are drawn and ideas for further works on diagnostic fulfilment and on the prognostic phase are presented.

# Chapter II

## Prognostic and Health Management

In this Chapter, the basic concepts of the Prognostic and Health Management are presented, in order to provide the reader with an overview of the aforementioned topic. This Thesis will be focused mainly on the initial step of the CBM/PHM process, that is, the fault identification through the system diagnosis, thanks to the results achieved from past thesis works and from several scientific papers.

### 2.1 Introduction to PHM

Over the past decades, a wide range of implementation strategies to perform the so-called *health management* continued to spread; they deal with the fault diagnosis and prognosis on critical systems in industrial, aerospace and automotive sectors, as reported in [1]. The aim of developing and implementing effective technologies for diagnosis and prognosis is to detect faults in their early stage, in order to be capable of acting promptly on the system. Fault isolation and diagnosis use detection events as the starting point for the classification of the fault within the system being monitored. Condition and failure prognosis predicts the *Remaining Useful Life* (RUL), i.e. the operating time between fault detection and an unacceptable level of degradation. Specific requirements in terms of confidence and severity, that is the accuracy of the process, must be declared for diagnosis and prognosis of a critical failure mode.

To specify fault detection and diagnosis accuracy it shall be used:

## **Prognostic and Health Management**

---

- the probability of anomaly detection, including false-alarm rate and real fault probability statistics;
- the probability of specific fault diagnosis classifications using specific confidence bounds and severity predictions.

For what concerns the prognosis accuracy, it must be first identified:

- the degradation level beyond which the operation is considered unsatisfactory;
- a minimum number of warning time to make available to the user required information that can be applied before the failure is encountered;
- a minimum probability level that RUL will be equal to or greater than the minimum warning level.

The design of the Prognostic and Health Management technologies is done by adopting the “designed in” approach, implemented within an integrated maintenance system that supports the equipment throughout its lifetime and provides a positive impact on safety, reliability and overall life-cycle-cost reduction. Moreover, the “designed in” approach is performed with the hardware design itself and thus acts as the process needed for system validation and managing changes, thanks to a continuous feedback of experience, evaluating system design improvements and trade-offs.

The main goal of the Prognostic and Health Management is to accurately forecast the fault/failure occurrence or the RUL of critical components and quickly isolate the root causes of failure, once that the latter has been detected. From this prospective, maximizing system availability and minimizing downtime through a more efficient problem-solving are of first importance. Furthermore, an integrated maturation environment is required for assessing and validating overall prognostics and health management accuracy. Hence, an approach could be quantifying the associated uncertainties at each individual level and build up the accumulated accuracies to be passed up to the system architecture. This process will be able to assess the decision-support reasoner algorithm, on the base of the ability to promptly detect and diagnose the fault causes and predict the RUL of the component and considering also the achieving of the overall operational goals, economic costs/benefits, etc.

The two main areas of interest of this methodology are the *Condition-Based Maintenance* (CBM) and the *Prognostics and Health Management* (PHM). The CBM is the use of the run-data extracted from the analysed system to determine its condition and thus its current fault/failure condition, usable to schedule required repair and maintenance before the breakdown occurs. The PHM handles the forecasting of future behaviours, in terms of current operating states, and the scheduling of required maintenance actions for system health. Thus, the CBM/PHM procedures are intended to deal also with the physics of the failure mechanism associated with the particular system or component, in order to understand which is the optimal choice in monitoring strategies, tools and algorithms to detect, isolate and predict the evolution of the fault.

*Failure Modes and Effects Criticality Analysis* (FMECA), dealing with *Reliability-Centred Maintenance* (RCM), determines the severity of failure modes, their frequency of occurrence and their testability. For each of them, FMECA considers fault symptoms and thus the required sensor to monitor their behavioural patterns. It may also define the optimal diagnostic and prognostic algorithm to address the identified failure modes.

The main modules of an integrated approach to CBM/PHM system design are shown in Figure 1, where the feedback loops are intended to optimize the process and complete the data collection, whereas the analysis steps are important inputs to the developments of the fault diagnostic and prognosis algorithms.

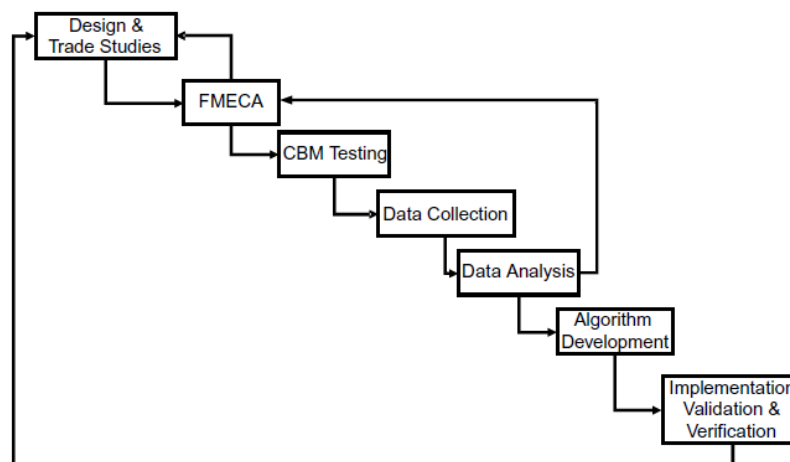


**Fig. 1** - An integrated approach to CBM/PHM design.

The general CBM/PHM cycle is shown in Figure 2. A preliminary offline phase is followed by an online implementation. The former deals with the background studies to be done before the online CBM implementation. They include the determination of the most important features for the system condition assessment, the FMECA, the collection of the machinery legacy data for a useful fault prediction and the specification of the particular resourced to perform maintenance actions. The online phase provides machinery data extraction from the sensor, signal pre-processing, identification of the most useful features for determining current status/fault condition, fault detection and classification, prediction of evolution fault and scheduling of required maintenance.

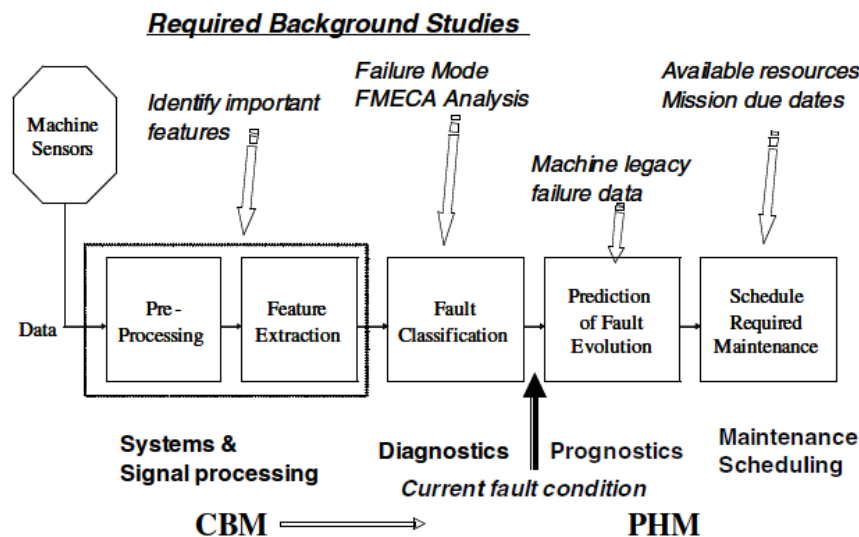


Fig. 2 – The CBM/PHM cycle.

The core of a good CBM/PHM system design is the understanding of the physics behind the failure mechanism and FMECA aiming to fulfil this goal. Indeed, FMECA study tries to relate failure events to their root cases (identifying failure modes) and their severity, frequency of occurrence and testability. Fault symptoms are related to the behaviour of the system under fault conditions, which are monitored and tracked by sensors and monitoring apparatus. The design of an FMECA must identify failure modes and classify them according to their severity, frequency of occurrence and testability. In particular:

- *Severity* ranks the failure mode according to its ultimate consequence (e.g. catastrophic, critical, marginal, minor);
- *Frequency of occurrence* distinguish classis of classification on the basis of mean time between failure (MTBF) ranges (e.g. likely, probable, occasional, unlikely);
- *Testability* indicates whether symptoms or indicators of a particular failure mode can be tracked via conventional or PHM sensors. Hence, it excludes from the candidate failure mode set the ones that cannot be measured.

After the FMECA, a CBM test is performed, whose objective is to design the required instrumentation, data-collection set, testing procedures. This test runs the system under controlled conditions on a test cell or under real operational regimes in order to acquire a baseline of fault data to be used to train and validate the diagnostic and prognostic algorithms.

For what concern the performance rating, a CBM/PHM system assists the maintainer to choose the optimum time to perform maintenance given a set of constraints, which determine confidence bounds on the availability of critical processes and tasks to meet production requirements. Moreover, the CBM/PHM system may also provide the user with operational capabilities, which guarantee a more fault tolerant, robust and reliable systems. It should be mentioned that also cost-benefit analysis studies are essential in deciding not only the technical pluses of these new technologies, but also their economic feasibility. After performing this analysis, technical and economic measures are weighted appropriately and put in a matrix form, in order to see clearly the possible benefits of the CBM system over its life cycle.

Performance metrics for fault diagnosis and prognosis functional elements are the main assessment of the CBM/PHM system, based on sound machinery, conditions monitory and statistical signal-detection techniques.

The verification and validation techniques for CBM/PHM technologies are implied, with the aim of ensure that delivered capabilities meet system design requirements, in accordance with system performance metrics. These techniques are intended to achieve system accreditation, that is, when the system accomplishes its performance requirements within stated system's constraints that have been determine by the offline

validation process. The system's performance could be checked by collecting actual or simulated data and asserting whether the designed or deployed system meets the specifications. Hence, the validation process involves extracting the action of the control code produced by CMB algorithm, in the form of Boolean expressions, and ensuring that those expressions satisfies the specifications.

### 2.1.1 Fault Diagnosis

Fault diagnosis, or *Fault Detection and Identification* (FDI), constitutes the initial step for the development of the CBM/PHM process. It deals with the detection of fault/anomaly condition, the isolation of the faulty components in a system or process, and the choice of the possible effect of a failing/failed component on the system's health. In general, useful information are extracted as feature/condition indicators (CIs) from a collection of data coming from various sensors. Then, they will be used as input to diagnostic routines, which will assert imminent failure conditions. The phases through which the fault diagnosis is performed are the following:

- *fault (or failure) detection*, where an anomaly operation condition is noticed and stated;
- *fault (or failure) isolation*, which determines the component that is failing or has already failed;
- *fault (or failure) identification*, which the nature and the extent of the fault (or failure) is determined.

A system- and application-dependent set of requirements is defined, since the fault diagnosis algorithms are referred to physical property of anomaly conditions, which changes through noticeable phenomena.

With the aim of estimating the RUL or the Time-to-Failure (TTF) of a failing component and improving the efficiency through the CBM, faults need to be accurately detected, without false alarms. Therefore, the diagnostic routines should be the best possible, minimizing the false positives/negatives and reducing the time delay between the initiation stage and the detection and isolation of the faulty condition.

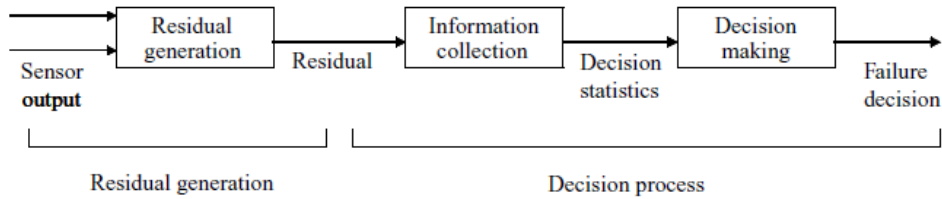


**Fig. 3** – General FDI structure.

A general FDI structure is presented in Figure 3. A residual signal, representing a deviation from the standard operating conditions, is generated by the comparison between a model output and the actual system output. The methods used for this purpose can be based on time signal statistics, system identification, frequency domain techniques, etc. Then, due to this residual signal, one takes decisions about the operating condition of the system. The typical technologies used in this early stage are the model-based and the data-driven methods. The former builds on an accurate dynamic model of the system and has the advantage of detecting even the unexpected faults, generating the residual signal that indicates a potential fault condition. Instead, the data-driven technique detects only the anticipated faults of a model constituted by a neural network that must be trained first with a data set coming from known prototype fault patterns and then launched online to detect and identify the faulty component.

The main component of the FDI procedure is the *fault-feature vector*, that is, a data set containing information about the system operating condition useful for determine the current fault status of the system itself. It is generated by means of model-base techniques, determining the parameter of the physical model using Kalman filters or recursive least squares, data-driven methods, using for example vibration frequency spectrum information, or statistical regression techniques acting on existing historical legacy data. Once built, the feature vector is employed as input to fault classification block, which contains different types of decision-making algorithms.

A basic concept for the fault detection is represented by alarm bounds of fault tolerance limits. As shown in Figure 4, they consist in predefined boundaries that indicates when an anomaly condition may be occurring. When the measured signal goes beyond these limits, an alarm state is activated. It must be taken into account that the signal itself has *confidence bounds* that should be considered in decision making of the diagnosis

process. There are two way for deriving fault tolerance limits: one consists in setting the bounds directly on current measured signal, whereas in some situations alarm bounds can be determined basing on available historical data and past observed failing situations.

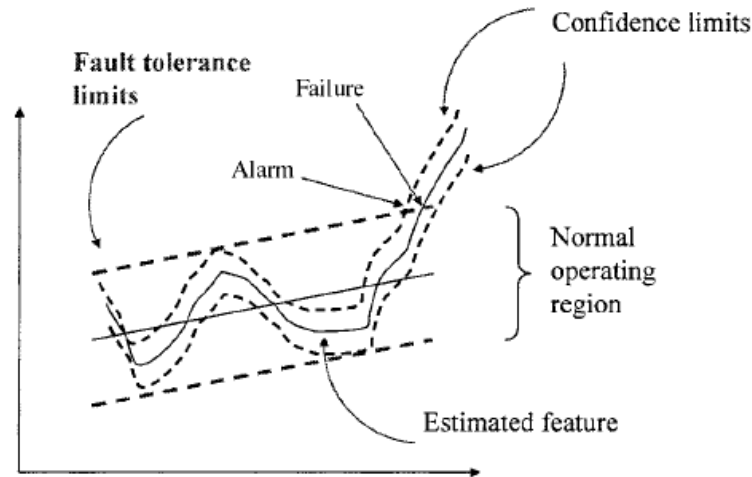


Fig. 4 – Alarm bounds on measured sensor signals.

The analysis conducted in this Thesis refers to a physical model-based method, which derives a good dynamic model of the system using physical modelling principles or parameter estimation and system identification methods.

### 2.1.2 Fault Prognosis

As defined in [1], *prognosis* is the ability to forecast accurately and precisely the Remaining Useful Life (RUL) of a failing component of the system. A long-term prediction of the fault evolution to the point that may result in a failure occurrence is related to uncertainty issues. Thus, an *uncertainty representation* is required, in order to model different types of uncertainties due to various sources, along with *uncertainty management*, which deals with methodologies and tools to narrow as more as possible the uncertainty bounds as more data are available. Moreover, a good fault prognosis requires accurate and precise probabilistic models of fault growth and a statistically

wide enough baseline of failure data for training, validating and tuning the prognostic algorithms. The main goal of the prognosis is to monitor and track the time evolution, that is, the growth, of the fault and predict the RUL after that an impending failure condition is detected, isolated and identified. Obviously, predictions about fault severity and impending failures are essential. An example of fault propagation is shown in Figure 5.

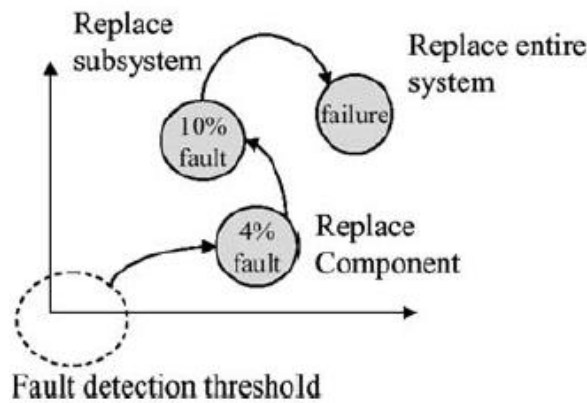


Fig. 5 – Fault propagation.

The class of prognosis schemes considered in the Thesis is the *model-based* one, which comprehend also the schemes employing a dynamic model of the predicted process. In general, this type of methods provide an approach to understand failure mode progression of the component. Physics-based models' implementation are capable to compute critical component damage as a function of operating conditions and to express the total effects in terms of component life employment. Then, integrating physical and stochastic modelling techniques, the presented model can be used for evaluating the RUL of the component as function of uncertainties in its particular fault conditions. Finally, the results coming from this model can be implemented for real-time failure prognostic predictions with specified confidence bounds. The physics-based model uses the critical and life-dependent uncertainties in order to examine the current health valuation and the future RUL predictions with respect to a risk level, as shown in Figure 6.

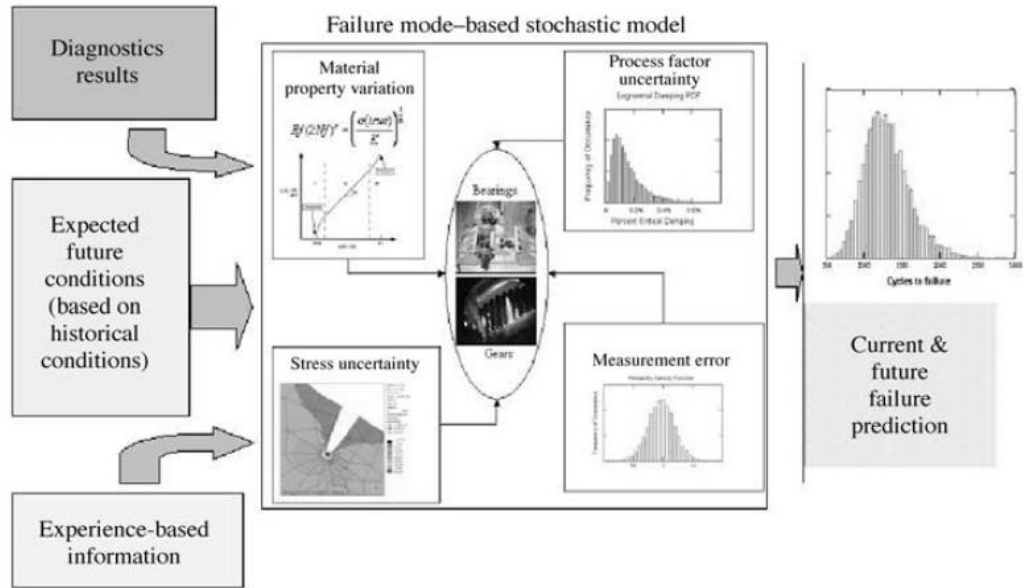


Fig. 6 – Physics-based modelling approach.

In order to perform the prognosis with a physics-based model, an operational profile prediction must be first developed using steady-steady state and transient online measurements. In this way, the probabilistic model of the critical component can be run, creating statistical simulations of the future operating profiles from the known statistics of the past ones. Then the nonlinear nature of many failure mechanisms depends on both intrinsic characteristics of the profiles and the operational mix.

The methodology used in the following part and presented here for the accurate prediction of a failing component is the one based on *particle filtering and learning strategies*. This approach considers two models, a state dynamic and a measurement one, to predict the future probability density function of a state for estimating the time evolution of a fault damage. Since the prediction, especially a long-term one, involves a great amount of uncertainty, one must consider critical state variables as random variables with related probability distribution vectors, through which the confidence intervals could be determined. One of the most suitable solutions to the prognosis problem is the recursive Bayesian estimation technique, that is, a method to combine both the information from fault growth models and online sensors data coming from the key fault parameters observation. If a timely detection and isolation of the fault is done, it is possible to consider the sensor data available for a certain “time window” that

allows improvements in model parameter estimations for an enhancement of the prediction. At the end of the time window, no additional adjustments are allowed.

In general, the probability density functions (PDFs) used in probabilistic methods are sufficient to forecast the quantities of interest in prognosis, since they can be extracted directly from observed statistical data. However, some probabilistic side aspects must be taken into account, such as manufacturing variability, mission history variations and life degradation as well as false alarm probability. A schematic representation is shown in Figure 7.

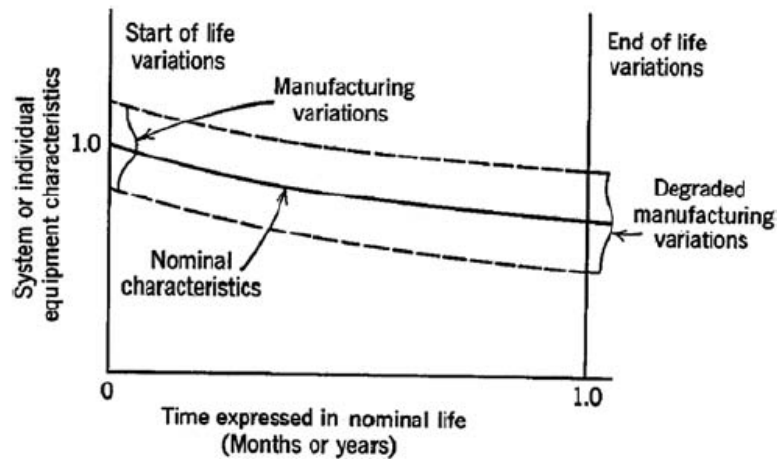
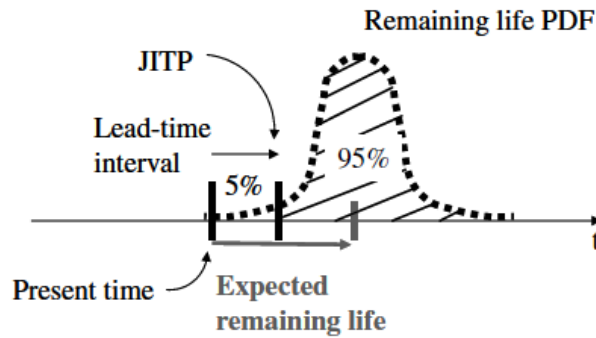


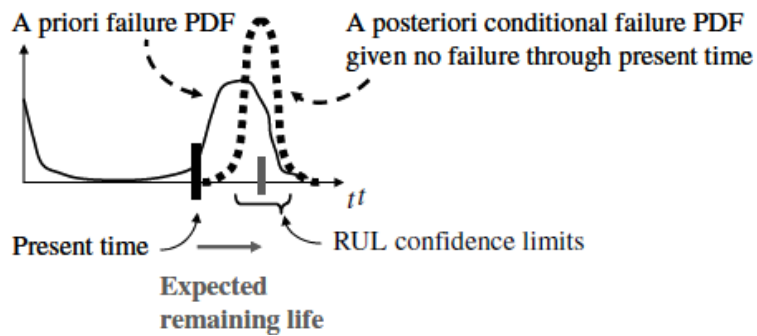
Fig. 7 – Manufacturing variability and mission history effects.

For what concerns the PDF of remaining useful life, a component must be relieved of service when a high probability of failure occurs. A comparison between the ideal and the real RUL PDF is reported in Figure 8. As depicted in (a), a just-in-time point (JITP) is defined in correspondence to a 95% probability that the component has not failed yet. Nevertheless, the RUL probability density function is a *conditional PDF* that changes through the time, that is, it must be recomputed at each time  $t$  according to the new data, which ensure that the component has not failed yet at that time. In (b) one starts with an a-priori PDF similar to the *hazard function*, i.e. a typical probability of failure curve. As time goes on, a recalculation of the a-posteriori RUL PDF is required, due to the fact

that the failure has not occurred yet, renormalizing the PDF at each time to obtain a unitary area.



(a)



(b)

**Fig. 8 – (a)** The RUL pdf and the Just-In-Time removal-from-service point; **(b)** the RUL pdf as time-varying conditional pdf.

After a while, as clearly shown in Figure 9, the variance of the RUL PDF decrease and the PDF becomes narrower, because approaching to the failure point one becomes more confident about the time of failure and the predicted time turn out to be more accurate.

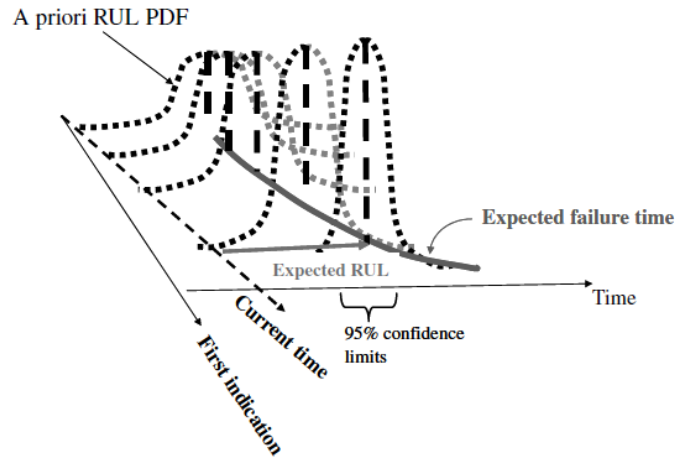


Fig. 9 – Time evolution of the RUL pdf.

### 2.1.3 Performance Metrics

After having introduced the fault diagnosis and prognosis characteristics, it is now important to assess the technical and economic feasibility of CBM/PHM systems, which should meet certain general requirements.

Further than this, for an effective fault diagnosis and prognosis process one must recur to feature selection and extraction metrics, before to select the optimal feature set. The goal is to differentiate, in the most clearly possible way, a certain fault condition from the others and from the healthy state of the system, with the maximum prediction accuracy. For this purpose, different actions are taken, such as the measurement of information, distance, dependence, etc.

Performance requirements for fault diagnosis algorithms mainly handle the maximum allowable percentage of false positives and false negatives of the total present faults over the system expected life. A trade-off between the two metrics is clearly needed, hanging in favour of a severer false-negative requirement, since the false negatives present the major risks to the system health and may even lead to catastrophic failures.

Another significant metric is the time-delay one, which provides the operator with an early alarm of an impending failure and supplies a wide-enough time window to perform the prognostic algorithm tasks.

In order to understand how well a fault is diagnosed, the *Receiver Operating Characteristic* (ROC) curve is chosen as an effective tool together with other types of metrics, such as the *ground-truth severity level*. This is a measure of the fault severity used as scaling factor for the ROC curve mapping, where confidence levels are also reported as a threshold metric.

Of more interest to this work, are the prognosis performance metrics. As already said, the results coming from the prognosis algorithms are the predicted time of failure and the confidence intervals, both to be considered. Furthermore, these measurements evolve with time as more data are available and thus the measures are expected to improve over time. Two main performance metrics are considered here: *accuracy*, that measures the closeness of the predicted value to the actual one, and *precision*, which indicates how much the predictions are clustered together, involving the confidence level and the prediction distribution.

- **Accuracy**

If the actual and predicted failure times for the  $i$ th experiment are  $t_{af}(i)$  and  $t_{pf}(i)$ , respectively. Then, the accuracy  $A(t_p)$  of the prognostic algorithm at a specific predicting time  $t_p$  is:

$$A(t_p) = \frac{1}{N} \sum_{i=1}^N e^{-\frac{D_i}{D_0}}$$

where  $D_i = |t_{pf}(i) - t_{af}(i)|$  is the distance between the actual and the predicted failure times,  $D_0$  is a normalizing constant based on the considered actual value and  $N$  is the number of the experiments.

The relationship clearly shows that the accuracy is higher when the predicted and the actual values are the same, whereas it becomes lower as the predicted values deviates from the actual one. Moreover, the measurement *sensitivity*, that is, the probability of detection given a fault, is very low when the predicted and the actual values deviates too much.

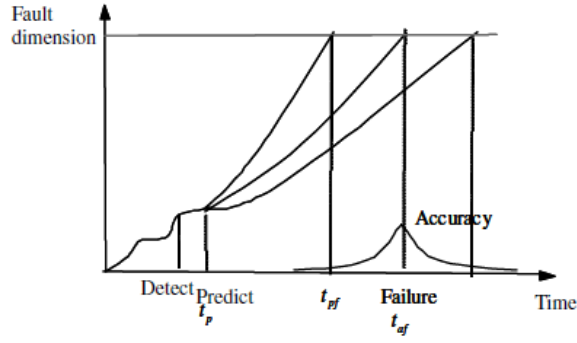


Fig. 10 – Predicted and actual failure times and the associated accuracy.

- **Precision**

The narrowness of the interval in which the RUL lies is defined according to the predicted results variance, since the precision increases as the predicted values are clustered together around the actual value and decreases as the predicted values are dispersed over the output range. Moreover, also the width of the confidence interval is an important aspect to be considered, because narrower confidence intervals give higher precision. An example of this is presented in Figure 11 and Figure 12.

Defining the *prediction error* as  $E_i = t_{pf}(i) - t_{af}(i)$ , its mean and variance values will be computed, respectively, from the following relationships:

$$\bar{E} = \frac{1}{N} \sum_{i=1}^N E_i$$

$$\sigma^2 = \frac{1}{N} \sum_{i=1}^N (E_i - \bar{E})^2$$

and the precision  $P(t_p)$  at a specific prediction time  $t_p$  is given by:

$$P(t_p) = \left( \frac{1}{N} \sum_{i=1}^N e^{\frac{R_i}{R_0}} \right) \times e^{-\frac{\sigma^2}{\sigma_0}}$$

where  $R_0$  and  $\sigma_0$  are the normalizing factors,  $R_i$  the prediction confidence interval for each experiment. The value of the prediction ranges from 0 to 1 (the highest).

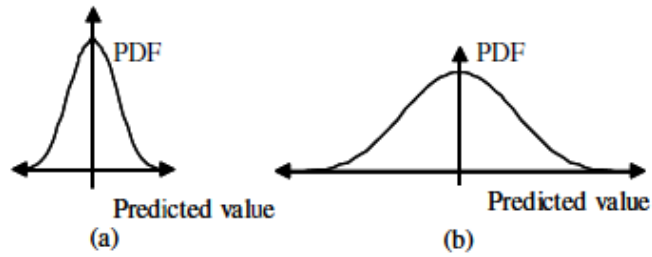


Fig. 11 – Prediction distribution related to precision: (a) higher precision output and (b) lower precision output.

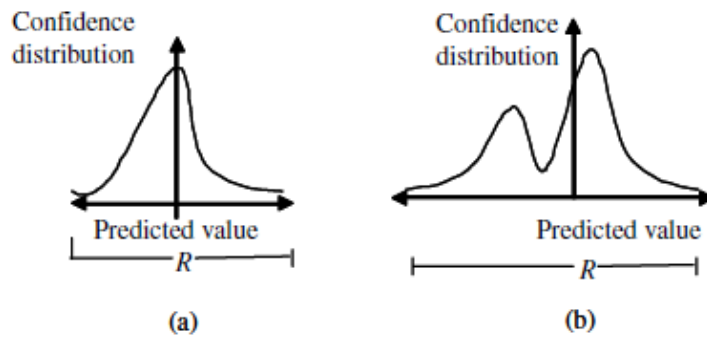


Fig. 12 – Precision dependency on prediction confidence bounds, R: (a) higher precision output and (b) lower precision output.

## 2.2 Prediction confidence metrics

During the prediction of fault occurrence, the inherent uncertainties must be considered and hence, uncertainty bounds are needed to be defined. In this regard, if at current time  $t_0$  a fault has been detected and isolated, then a prognostic routine will forecast the mean time to failure  $T_{fm}$ , the earliest time to failure  $T_{fe}$ , and the least time to failure  $T_{fl}$ . The time to failure is the PDF relative position along the  $t$  axis with respect to the incidence of the actual failure. The hazard line specifies the fault dimension at which the stops its optimal working condition, i.e. when the failure occurs, as shown in Figure 13. These failure data are available to superimpose one or more distributions, which could be either possibilistic functions or probability density functions.

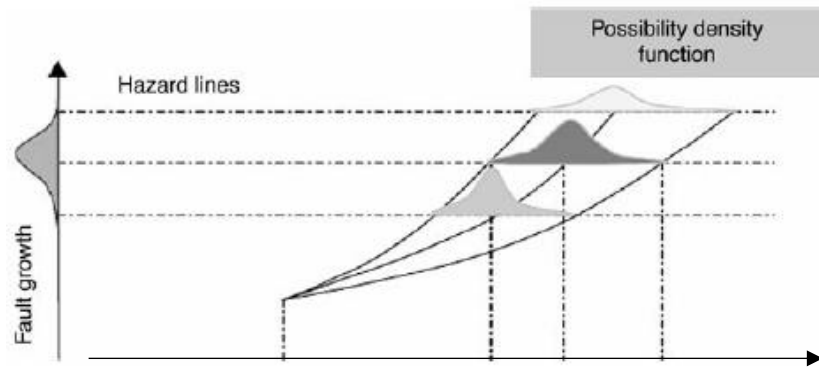
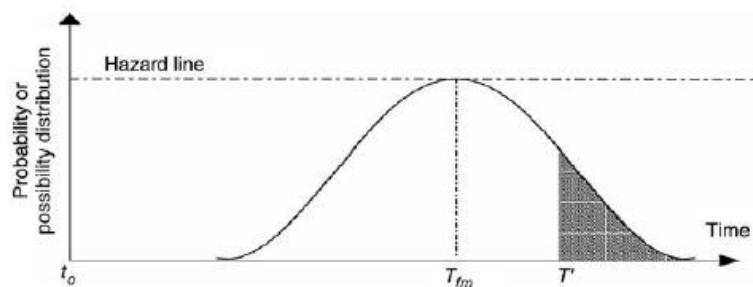
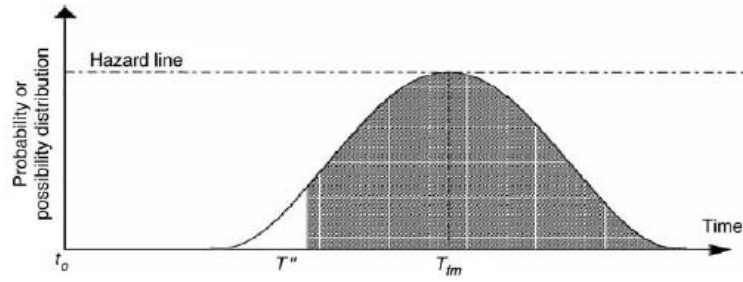


Fig. 13 – Possibility density function for confidence bounds.

Furthermore, in Figure 14 is represented the distribution at  $T_{fm}$  that crosses the hazard line. Here the mission entails the availability of the set at hand for time  $T'$ . The integral under this distribution from  $T'$  to infinity represents an estimation of the asset probability to not fail before the mission is completed. Then, specifying a certain confidence level a new time limit for fault occurrence  $T''$  is defined and so on, thus arriving at the length of time the asset will be available within the required confidence limit. This can be seen as a dynamic evolution of the estimation, that is, as more data become available in the passing of time, uploaded confidence level are derived and the uncertainty bounds will shrink as much as possible.



(a)



(b)

Fig. 14 – Time evolution of the distribution at the hazard line.

### 2.3 Advantages of using PHM

As already said in the Section 2.1, the PHM is a particular technique, which allows to identify the presence of a defect before a failure occurs (based on signals available within the system at hand), to classify the detected defect, and to forecast its future evolution estimating the Remaining Useful Life and the Time-to-Fault of the device. Therefore, in order to overcome the reliability problems of the modern EMAs, building a solid PHM system could be a possible solution to cope with these issues. An example of the PHM strategies is depicted in the Figure 15. Once an incipient failure or fault is detected with specified confidence, the prognostic algorithm is initiated to predict the fault's time evolution. Thus, the final state of the system acts as the initial condition for prognosis [2].

The advantages of a predictive maintenance rather than a close-to-breakdown one, are the growth of the system reliability and the reduction of serious damages, that could lead to failures spread in different parts of the system. Moreover, the PHM strategy optimizes the trade-off between costs and system efficiency, fully exploiting the useful life of the system and, consequently, scheduling the maintenance activities in order to guarantee the maximum system capacity.

In this Thesis, only the Fault Detection Identification for the diagnosis phase is explored.

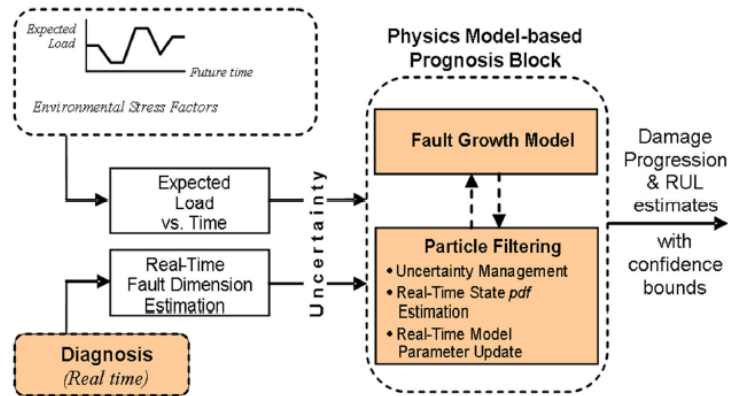


Fig. 15 – The Prognostic Framework<sup>1</sup>

<sup>1</sup> A. De Martin, G. Jacazio, and G. Vachtsevanos, “Anomaly Detection and Prognosis for Primary Flight Control EMAs”, European Conference of The Prognostic and Health Management Society, 2016, p.7.

# Chapter III

## Fault Tolerant Control

In this Chapter, the Fault Tolerant Control (FTC) technique is seen in detail. This type of reconfigurable control methodology consists of a three-level architecture. The *low-level* is investigated in this Work, in which the Model Predictive Control (MPC) routine is used for the reconfiguration in the case of fault detection. It is able to trade-off between the Remaining Useful Life (RUL) of the component and its performance. The intent of this study is to introduce the control methodology of Model Predictive Control, taking advantage of the fault diagnosis and prognosis routines developed at the component level. In particular, prognostics information is included in the MPC cost function to be minimized, in order to mitigate the faulty conditions of the system. This control design compared with existing production controllers could lower its impact on the system and, mostly, it is a very adaptable approach.

### 3.1 Introduction to Reconfigurable Control

As seen in Chapter II, the health diagnosis and prognosis of a machine consist of detection and localization of the fault and estimation of the remaining life of the faulty component. However, the health prognostics used so far usually provides short-term life prediction, as it is triggered by the detection of anomalous behaviours that indicate there is already noticeable damage in the component. The aim of the recent studies has been to integrate prognostics with control. In fact, one of the possible purposes to extend the component lifetime is to change control strategies. This idea focuses on long-term life

prediction and control, since the innovative controller embeds the remaining useful life information coming from prognostic routines as a controlled parameter and the controller applies novel adaptive control algorithms for guaranteeing the desired long-term life [13].

*Fault-Tolerant Control (FTC)* is one of the new control technologies that is intended to manage incipient failure and preserve a stable system operation for all the emergency duration. These PHM-based control methods present an active reconfiguration of the control law considering the failure prognostic information. In general, FTC technologies have two main goals: Fault Detection and Isolation and Control Reconfiguration. The latter deals with the lowest of the three tasks levels of the FTC. The main elements of the Control Reconfiguration architecture are described in [2] and are presented in Figure 16.

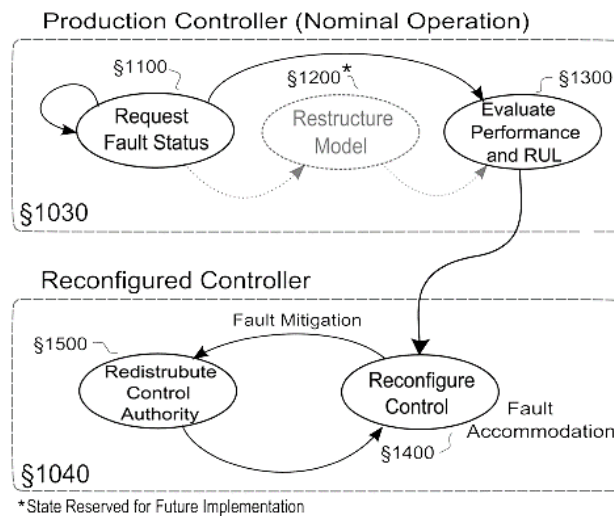


**Fig. 16** – State transition diagram for low-level reconfigurable control.<sup>2</sup>

The control architecture is comprised of two controllers: the original production controller (§1030) and the reconfigured controller (§1040). Initially, the production

<sup>2</sup> D. Brown, G. Georgoulas, B. Bole, H. Pei, M. Orchard, L. Tang, B. Saha, A. Saxena, K. Goebel, and G. Vachtsevanos. "Prognostics enhanced reconfigurable control of electro-mechanical actuators." In Annual conference of the prognostics and health management society, pp. 1-17. Rochester, NY: PHM Society, 2009.

controller is utilized while diagnostic routines continuously monitor the system for one, or more, fault modes (§1100). Once a fault is detected, the RUL requirements are checked to assess if the requirements can be accomplished without control reconfiguration (§1300); if not, the MPC routine is reiterated (§1400). It should be pointed out that, in the presence of an incipient failure, the system dynamics remain essentially the same. This assumption is valid when the incipient failure or fault is detected at an early stage of its beginning and evolution and thus, has not deeply affected the actuator dynamics. Under these conditions, the restructure of the system dynamics is not necessary in the control formulation. However, if the fault significantly influences the system dynamics, then a restructuring step (§1200) can precede the reconfigurable control routine so the current state of the system is reflected in the control formulation.

## 3.2 Model Predictive Control

The *Model Predictive Control* (MPC) designates a wide range of control methods, which use process models to obtain a control signal through the minimization of critical parameters. The main idea behind these methods is to use a model to predict the process output at future time instants, which constitute the so-called *prediction horizon*, and to compute a control sequence, which minimizes an objective function. Then, it implements the *receding strategy* at each instant in order to shift the horizon towards the future, applying the first sequence control signal calculated at each step.

The good performance of the MPC technique highlights its capacity to achieve highly efficient control systems able to operate during long periods. The MPC shows to be a valid strategy for industrial control, although the initial lack of theoretical information at some critical points such as stability and robustness.

Some of the advantages of the MPC with respect to other methods are, for example, its relatively easy tuning, even with only a limited knowledge of control, its implementation in a great variety of processes, the introduction of feed-forward control to compensate the measurable disturbances, etc.

However, the MPC strategy has also its drawbacks, such as the complexity of the control law, although it is easy to implement, the need for an appropriate model of the process to be available, the discrepancies existing between the real process and the model used that could affect the algorithm designed on a prior knowledge of the model itself, etc.

### 3.3 MPC Strategy

The basic concept behind all the MPC controllers is described accurately in [3] and is characterized by the following steps:

- i. The future outputs for a given horizon  $N$ , called the *prediction horizon*, are predicted at each instant  $t$  using the process model. These predicted outputs  $y(t + k | t)$  for  $k = 1 \dots N$ , i.e. the values of the variable  $y$  at the instant  $t+k$  calculated at the instant  $t$ , depend on the known values up to instant  $t$  (past inputs and outputs) and on the future control signals  $u(t + k | t)$  for  $k = 0 \dots N - 1$ , which are the one to be sent to the system and to be calculated.
- ii. The set of the future control signals is calculated by optimizing a determined criterion in order to keep the process as close as possible to the reference trajectory  $w(t + k)$ , which can be the set point itself or a close approximation of it. In general, this criterion takes the form of a quadratic function of the error between the predicted output signal and the predicted reference trajectory. The control effort is usually included in the objective function. If the criterion is quadratic, the model is linear and there are no constraints, an explicit solution can be achieved; otherwise, an iterative optimization method is adopted.
- iii. The control signal  $u(t | t)$  is sent to the process whereas the next control signals calculated are rejected, since at the next sampling instant  $y(t + 1)$  is already known and step 1 is repeated with this new value and all the sequences are brought up to date. Therefore, the  $u(t + 1 | t + 1)$  signal, which could be different from

$u(t + 1 | t)$  due to the new information available, is calculated following the *receding horizon* technique.

Therefore, the MPC controller is actually a *discrete-time* controller, which acts at regularly spaced, discrete time instants. The *sampling instants* are the times at which the controller acts, whereas the interval separating successive sampling instants is the *sampling period*  $\Delta t$ , also called the *control interval*.

As shown in Figure 17, the state of a certain SISO MPC system that has been running for many sampling instants, where integer  $k$  represents the current instant. The latest measured output  $y_k$  and previous measurements  $y_{k-1}, y_{k-2}, \dots, y_{k-N}$  are known and are represented by the filled circles in (a), while the controller previous moves  $u_{k-1}, u_{k-2}, \dots, u_{k-N}$  are represented in the same way in (b). Notice that, if there is a measured disturbance, its current and past values would be known. A *zero-order hold* receives each control move from the controller and holds it until the next sampling instant, causing the stepwise variations.

Then, the optimal moves are portrayed as the four open circles in (b), and the controller predicted output values are the open circles in (a). Notice that both are within their *constraints*, that are,  $u_{min} \leq u_{k+j} \leq u_{max}$  and  $y_{min} \leq y_{k+i} \leq y_{max}$ .

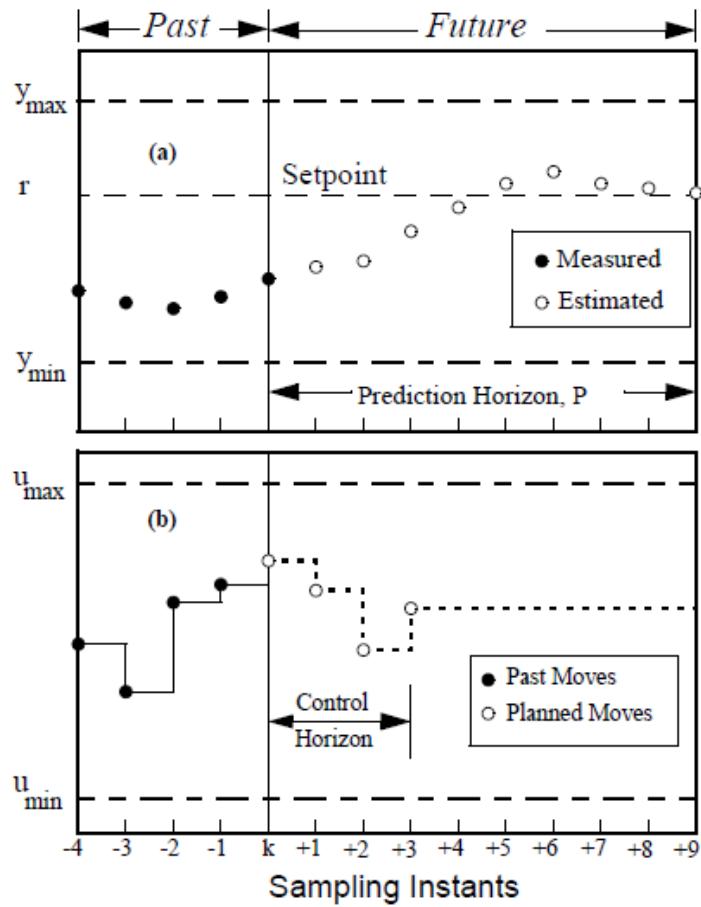


Fig. 17 - MPC controller state at the k-th sampling instant.

Now, in order to implement the current strategy, the basic structure is shown in the Figure 18, where is represented the model used to predict the future plant outputs, on the basis of past and current values and of the proposed optimal future control actions. The latter are calculated by the optimizer bearing in mind the cost function (where the future tracking error is considered) and the constraints. Thus, the choice of the process model is very important, since it must be able of taking out the process dynamic as well as precisely predicting the future outputs, in order to be easily implemented or understood.

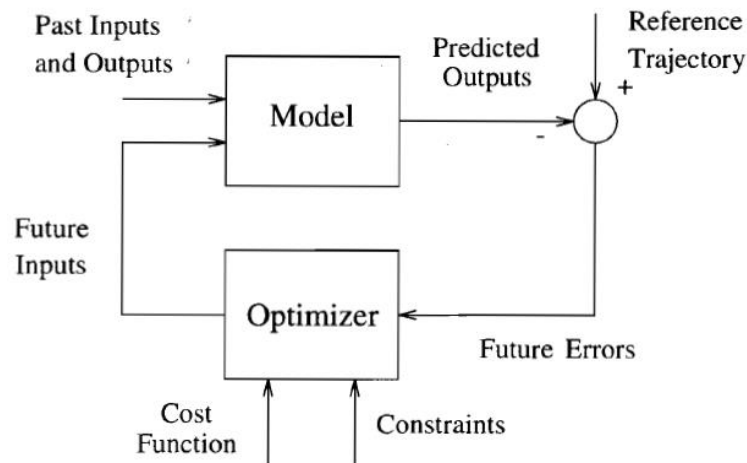


Fig. 18 – Model Predictive Controller structure

Amongst the many types of models used for different formulations, the Transfer Function model is maybe the most used one in the control design method, since its representation requires only a few parameters and is valid for all kind of processes, whereas the State-Space model is mainly used to describe multivariate processes.

The control actions are provided by the optimizer, which constitutes another important part of the MPC strategy. If the cost function is quadratic, its minimum will be in the form of an explicit linear function of past inputs and outputs and the future reference trajectory. Otherwise, in the presence of inequality constraints the solution can be obtained through more computationally complex algorithms. The size of the optimization problem is due to the number of variables and to the prediction horizons used and, in general, it is relatively modest to be solved. However, the amount of time needed for solving the constrained and robust cases can be much higher than that needed for the unconstrained cases. Thus, the process bandwidth to which constrained MPC can be applied is significantly reduced.

### 3.3.1 MPC Controller Model

The model that could be adopted for the electromechanical actuator under consideration and shown in detail in the next chapter, is a high-fidelity 5th order state-space model [2], which can be expressed by the linear state-space system  $(\mathbf{A}_m, \mathbf{B}_m, \mathbf{C}_m)$ . It is employed to relate the control inputs and measured outputs of the actuator to the internal system states of the brushless AC (BLAC) motor,

$$\begin{cases} \dot{\tilde{\mathbf{x}}}_m = \mathbf{A}_m \tilde{\mathbf{x}}_m + \mathbf{B}_m \mathbf{u}_m \\ y_m = \mathbf{C}_m \tilde{\mathbf{x}}_m \end{cases}$$

where  $\tilde{\mathbf{x}}_{m0} = \tilde{\mathbf{x}}_m(0)$ . The internal state of the system is defined by  $\tilde{\mathbf{x}}_m = [\tilde{i}_m \tilde{\theta}_m \tilde{\omega}_m \tilde{\theta}_l \tilde{\omega}_l]^T \in \mathbb{R}^5$ , that is constituted, respectively, by motor current, motor position, motor speed, load position and load speed. The control input is defined by  $\mathbf{u}_m = [\theta_{ref} T_m T_{load}]^T \in \mathbb{R}^2$ , i.e. by the reference position, the mechanical friction torque and the external load disturbance; finally, the control output is defined by  $\mathbf{y}_m = [\theta_l i_m]^T \in \mathbb{R}^2$ , i.e. by the load position and the motor current.

The transition matrix  $\mathbf{A}_m \in \mathbb{R}^{5 \times 5}$  is defined accordingly the following representation

$$\mathbf{A} = \begin{bmatrix} \frac{-R}{L} & \frac{-k_{p1}k_{p2}}{L} & \frac{-k_e - k_{p1}}{L} & 0 & 0 \\ 0 & 0 & 1 & 0 & 0 \\ \frac{k_t}{J_m} & \frac{-k_{cs}}{J_m N_{cm}^2} & \frac{-b_m}{J_m} & \frac{k_{cs} N_{cl}}{J_m N_{cm}} & 0 \\ 0 & 0 & 0 & 0 & 1 \\ 0 & \frac{k_{cs} N_{cl}}{J_l N_{cm}} & 0 & \frac{-k_l - k_{cs} N_{cl}^2}{J_l} & \frac{-b_l}{J_l} \end{bmatrix}$$

where  $k_{cs}$  is the coupling stiffness,  $k_l$  is the load stiffness,  $k_e$  and  $k_t$  are respectively the back-emf and the torque coefficients,  $k_{p1}$  and  $k_{p2}$  are the controller gains,  $J_l$  and  $J_m$  are the load and motor inertias,  $L$  is the motor inductance,  $R$  is the motor resistance,  $N_{cl}$  and  $N_{cm}$  are respectively the load and the motor coupling coefficient.

It must be noticed that, in this case, in order to consider the type of error investigated in this study (i.e. static rotor eccentricity), the back-emf coefficient  $k_e$  must be modified. In fact, it must consider also the airgap variation and, therefore,  $k_e$  will be taken as an airgap variable and not as a constant, as shown later.

The control and observation matrices  $B_m \in \mathbb{R}^{5 \times 3}$  and  $C_m \in \mathbb{R}^{2 \times 5}$  are defined, respectively as:

$$B_m = \begin{bmatrix} \frac{k_{p1}k_{p2}N_{cm}}{LN_{cl}} & 0 & 0 & 0 & 0 \\ 0 & 0 & 0 & 0 & \frac{-1}{J_l} \end{bmatrix}^T$$

$$C_m = \begin{bmatrix} 0 & 0 & 0 & 1 & 0 \\ 1 & 0 & 0 & 0 & 0 \end{bmatrix}$$

Considering the described model for the EMA, the RUL can be increased by lowering the applied motor current  $i_m$ . However, since the motor current cannot be directly suited, it can be indirectly controlled by acting on the reference input  $\theta_{ref}$ , that is, the reference position of the electric motor. Therefore, the aim of the MPC is to compute the optimal  $\tilde{\theta}_{ref}$  for a given RUL and performance requirements.

### 3.3.2 MPC Implementation

The purpose of the control reconfiguration is to change the operating conditions (mainly through manipulated variables (MVs) to avoid the static eccentricity fault dimension reaching the given hazard zone before the time of mission completion  $t = t_{mission}$ . The reconfiguration of the control mechanism will guarantee the mission completion within the given time, though may cause some performance degradation.

In order to implement the new control algorithm in the simulation ambient, one can use the MPC control Toolbox of *The MathWorks, Inc.* [4].

The MPC method makes use of a target system, namely the *plant*, by combining prediction and control strategy. An approximate linear plant model provides the prediction. The control strategy compares predicted plant states to a set of objectives, and then adjusts available actuators to achieve the objectives fulfilling the plant *constraints*, such as actuator physical limits, boundaries of safe operation and lower

limits for product quality. In particular, in this study the plant is represented by the physical EMA system, that will be presented in the next chapter.

Primarily, a SISO (Single Input-Single Output) plant shown in Figure 19 is considered.

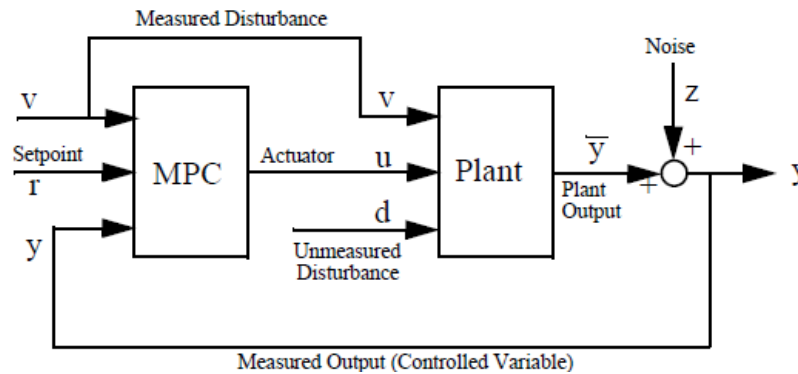


Fig. 19 – Block diagram of the MPC with plant and signals

The main goal is to hold a single *output*, that is, the *controlled variable*  $\bar{y}$ , at a *reference value* (or *set point*)  $r$ , by adjusting a single *manipulated variable* (or *actuator*)  $u$ . The block labelled *MPC* represents an MPC Toolbox feedback controller designed to achieve the control objective.

The SISO plant may have multiple inputs beyond the manipulated variable  $u$ , since there may also be the *measured disturbance*  $v$  and the *unmeasured disturbance*  $d$ . The unmeasured disturbances signal is always present: it is an independent input, not affected by the controller or the plant and represents all the unknown, unpredictable events that upset plant operation or the unmodeled dynamics. The only indication of the occurrence of these events is their effect on the *measured output*  $y$ , which is fed back to the controller, in order to compensate these disturbances. On the contrary, the measured disturbance  $v$  is another independent input that is directly received by the controller, allowing an immediate compensation for  $v$ 's impact rather than waiting until the effect appears in the  $y$  measurement thanks to a *feedforward* control. The feedforward/feedback actions include the controller *regulator* mode, whereas a *servo* mode can be also provided, adjusting  $u$  in order to track a time varying set point. The tracking accuracy depends on the plant characteristics, its constraints, the accuracy of

the model and whether future set point variations can be anticipated or not, precisely using the feedforward compensation.

Now, focusing on the case studied, the functionality of the MPC routine for RUL adaptation includes prognosis-based constraints on the internal states  $x_{min}^{RUL}$  and  $x_{max}^{RUL}$  as “soft” constraints. When the latter are initialized, the RUL (i.e. the results coming from the PHM routines) of the failing motor is evaluated and the RUL requirements are checked to assess if they are compliant to the reference values or not. If not, the soft constraints are updated to ease system performance requirements in the MPC. Then, the MPC computes the next control sequence. After control sequence application, the updated performances are evaluated and compared to the required ones. If the performance requirements are satisfied, the control sequence is reiterated. Otherwise, if the requirements are not satisfied or the soft boundaries can no longer be adapted, a control redistribution algorithm is activated [2].

# Chapter IV

## Test Bench Components

The novel methodology of the fault-tolerant control previously presented is applied for the design of critical subsystems, such as the Electromechanical Actuators (EMAs), taking advantage of online, real-time estimates of the RUL or static eccentricity fault of the failing component. It reconfigures the control action by trading-off system performance with the new control activity.

This Chapter examines the main components mounted on the test bench for flight control, whose model will be considered during the operational part. The basic characteristics of the EMA are presented thereafter, together with the description of the Simulink model used for simulation activities.

### 4.1 Electromechanical Actuators

The development of reliable electrical actuators for space and aeronautical applications has been recently implemented to eliminate hydraulic systems from aircraft and spacecraft, to improve safety, efficiency, reliability, and maintainability. Moreover, the increase in fuel costs, the aim to minimize the carbon footprint due to a greener consciousness and the emergence of new competitors have recently driven the aerospace industry to take steps towards creating environmental-friendly, safer and cheaper solutions. Another reason that has contributed to the progress of conventional aeronautical and space applications is the necessity to reduce the energy consumption

of hydraulic, mechanical, pneumatic and electrical counterparts of the actuators, referred as secondary power sources, which is approximately 5% of the total fuel burnt during the flight [5]. Therefore, in the past few decades, *more-electric* technologies take hold, especially in terms of secondary power sources, where the presence of traditional hydraulic, pneumatic and mechanical systems is being progressively reduced and replaced by electrical counterparts.

One of the most promising solutions for flight control actuation consists in the substitution of the heavy and not very versatile hydraulic systems with electrically powered actuators, namely the electromechanical actuators (EMAs). For examples, commercial aircraft such as Boeing 787 and Airbus A380 adopt EMAs for, respectively, landing gear brakes, spoiler surfaces and for actuating the slats. In these type of actuators, the electric power feeds an electric drive, which is mechanically coupled to a reduction drivetrain (e.g. gearbox and/or ball screw), placed between the electric drive and the flight control surface. Thus, mechanical power is locally generated for driving the flight control surface. Among all the electrical machines introduced in aerospace applications, permanent magnet synchronous machines (PMSMs) are a common choice for EMAs since they are characterized by high-power density and excellent efficiency.

However, even if EMAs represent a key technology, which is gaining interest due to its higher efficiency and further weight reduction, they are not yet sufficiently mature to fully replace conventional hydraulic servo-actuators' safety-critical functions, such as the aforementioned flight control. As reported in [6], several studies still need to overcome weight and size constraints for integration, voltage spikes and current transients affecting the stability of electrical networks, heat rejection for actuator thermal balance, reduced reflected inertia for dynamic performance, increased service life and fault tolerance or resistance for servo-actuators safety.

In the next paragraphs, a description of the EMA used in this study is provided, together with a usual fault affecting it, which is the bearing fault due to the presence of static eccentricity.

## 4.2 Components description

The test bench considered from now on is located in the DIMEAS laboratory of Politecnico of Turin and it has been studied started from [7]. Although it has been thought for flight control, here it is used for more general purposes applicable to a wide range of industrial aims. In Figure 20 is illustrated the typical architecture of the considered electromechanical actuator.

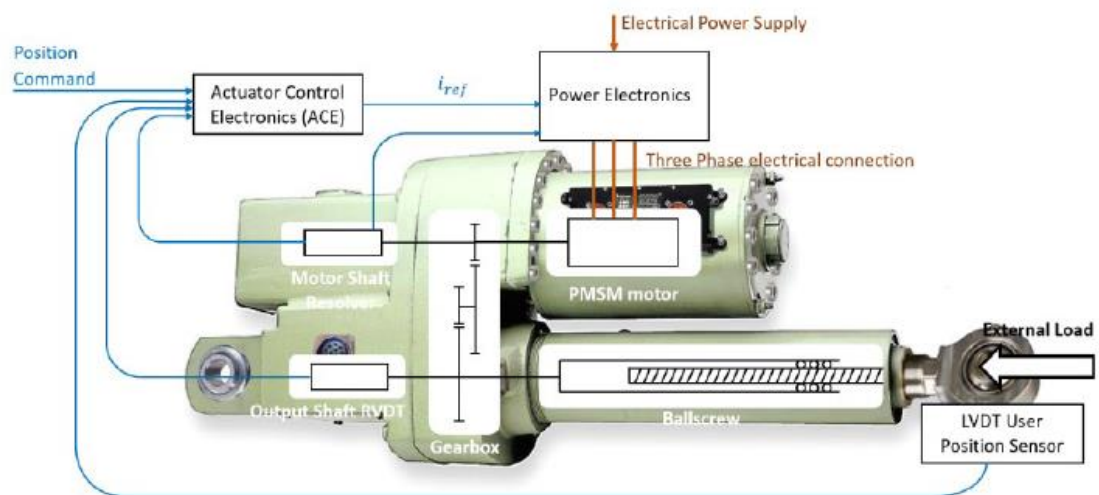


Fig. 20 – Typical architecture of an electromechanical actuator for flight controls.<sup>3</sup>

The actuator is a linear electromechanical cylinder (*LEMC*), whose electric part consists of a *Lenze* Permanent Magnets Synchronous Motor (PMSM). As one can see from the figure, the EMA architecture involves an Actuator Control Electronics (ACE) module, which compares the position command to the actual position measured by sensors, to compute a current command for the Power Electronics module. Then, this module converts the DC or AC electrical power supply into the required three-phase power for the PMSM, with the required frequency and amplitude depending on the command and

<sup>3</sup> P.C. Berri, M. D.L. Dalla Vedova, P. Maggiore, F. Viglione, “A simplified monitoring model for PMSM Servo-actuator prognostics”, MATEC Web of Conferences 304, 04013, EASN, 2019.

## Test Bench Component

---

rotor angular position. A mechanical transmission connects the motor to the controlled component on which an external load is applied. The transmission here consists in a planetary reduction gearbox and a device for converting rotary motion into linear motion. For this purpose, SKF rollers-screw are the main choice for their higher efficiency, lower backlash and higher specific load. A resolver on the motor shaft is needed for actuating the commutation sequence, while Rotary Variable Differential Transducers (RVDTs) or Linear Variable Differential Transducers (LVDTs) on the transmission output provide absolute position information for the control loop. Current sensors are used for closing the inner current loop and provide torque control, while the motor speed can be measured by a dedicated sensor or computed as the derivative of motor position.

The main data for the LEMC are taken from [7] and reported in Tab.1.

**Tab.1** –LEMC 2105 general parameters.

<b>Data</b>	<b>Value</b>	<b>UoM</b>
Type of screw	Roller screw	/
Crew diameter	21	mm
Screw pitch	5	mm
Max axial force	$40 \times 10^3$	N
Max input torque	41.7	Nm
Max linear speed	500	mm/s
Max angular speed	6000	rpm
Max acceleration	6	$m/s^2$
Actuator stroke	100	mm
Screw friction	$1.45 \times 10^{-4}$	$Kgm^2$

### 4.2.1 EMA Configuration and Working Principle

The servomotor evaluated in this Thesis is an AC sinusoidal brushless (BLAC) electric motor, using a resolver for motor commutation and supplied through its own EPU. It is interconnected with a mechanical transmission composed by a satellite gearbox and a roller screw. The motor nominal data are shown in Tab.2.

**Tab. 2** – Electric Motor rated data.

<b>Data</b>	<b>Value</b>	<b>UoM</b>
Rated speed $n_N$	1950	rpm
Rated torque $M_N$	5.5	Nm
Max torque $M_{max}$	18	Nm
Rated power $P_N$	1.1	kW
Rated current $I_N$	2.6	A
Max current $I_{max}$	10	A
Rated voltage $V_{N AC}$	345	V
Rated frequency $f_N$	130	Hz
Motor efficiency $\eta\%$	79	%
Motor inertia $I_M$	4	Kgcm <sup>2</sup>
Voltage constant $k_e$	1.31	V/(rad/s)
Stator resistance $R_s$	5.8725	$\Omega$
Rated inductance $L_N$	52.2	mH
Torque constant $k_t$	2.34	Nm/A
Max speed $n_{max}$	6000	rpm

The working principle of an electrical motor is based on the attraction between the magnetic fields obtained by a three-phase current alimentation of the three windings of the stator, symmetrically distributed at 120°. The rotor is composed by permanent magnets (PM) generating a flux  $B_r$  that will be dragged synchronously by the stator flux  $B_s$  obtaining a magnetic torque represented by the Eq. (1):

$$T_m = B_r B_s \sin(\theta) \quad (1)$$

where  $\theta$  is the *load angle* between the stator and rotor fields. The maximum value of  $T_m$  is obtained for  $\theta = 90^\circ$ .

The brushless motor presents a commutation, that is, the changing in the current inside the motor phases, made by an electric driver, instead of a brush and collector system as in the classical electrical motor. The synchronous AC motor is operationally similar to the brushless DC one, but they present some differences due to the back electromotive force (EMF) waveform and due to the torque ripple. The DC motor presents a trapezoidal back EMF, owed to a linear distribution of the conductors; instead, the AC motor waveform is sinusoidal, due to a sinusoidal distribution with more layers and a smaller coils span. Moreover, the AC motor conductors distribution guarantees a more fluid and noiseless commutation with a consequent reduction of the torque ripples.

Another difference between the two motors relies in the electronic control: in the DC brushless motor, a Hall sensor and a tachometric dynamo are used for rotor position and speed control, respectively, while the sinusoidal AC motor adopts a *resolver* for both rotor position and speed control.

A more specific description of the current commutation is described in the Figure 21.

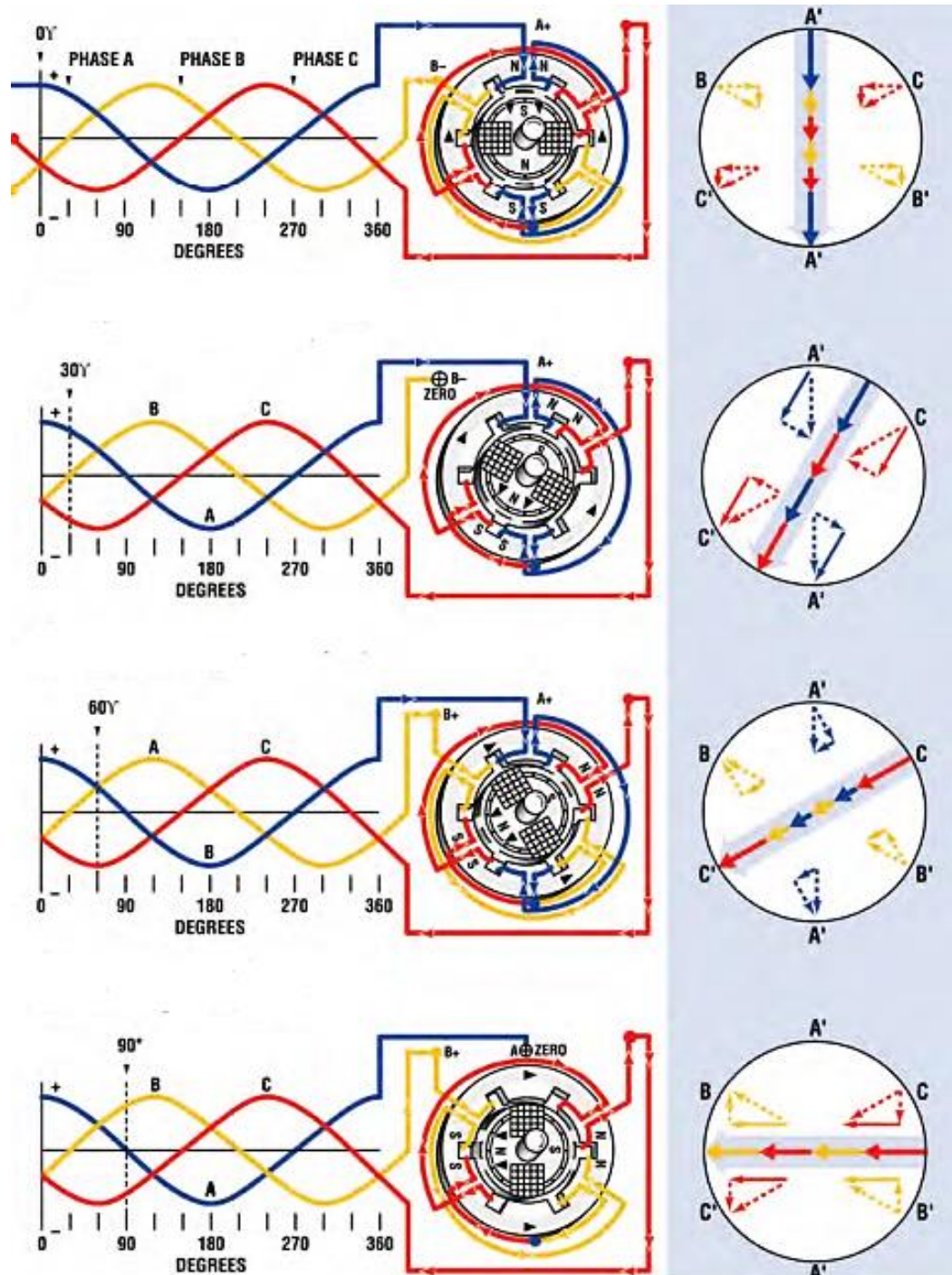


Fig. 21 – Ac motor. Three-phase power supply for a two-pole synchronous motor at 0°, 30°, 60°, 90°. <sup>4</sup>

<sup>4</sup> EM Weg Group, “The ABC’s of Synchronous Motors”, 09 December 2019, <https://static.weg.net/medias/downloadcenter/hfe/hf4/WEG-the-abcs-of-synchronous-motors-usaem200syn42-brochure-english.pdf>.

The AC motor mechanical torque  $T_m$  is expressed by the equation:

$$T_m = \frac{E \cdot I_m}{\omega}$$

where  $E$  is the back EMF and  $I_m$  the armature current. In order to obtain a constant  $T_m$  and to avoid torque ripples, both  $E$  and  $I_m$  must be sinusoidal. Besides, the dependence of the torque on the currents  $I_m$  constitutes a limit for  $T_m$  initial control. A solution to this problem could be returning to the DC motor case, and so decomposing the current into its components, which generate the flux and the torque, respectively. Therefore, the Field Oriented Control (FOC) is used for this purpose. It relies on an algorithm that allows controlling the current in the three phases of the motor and, consequently, the vector components of the stator magnetic field.

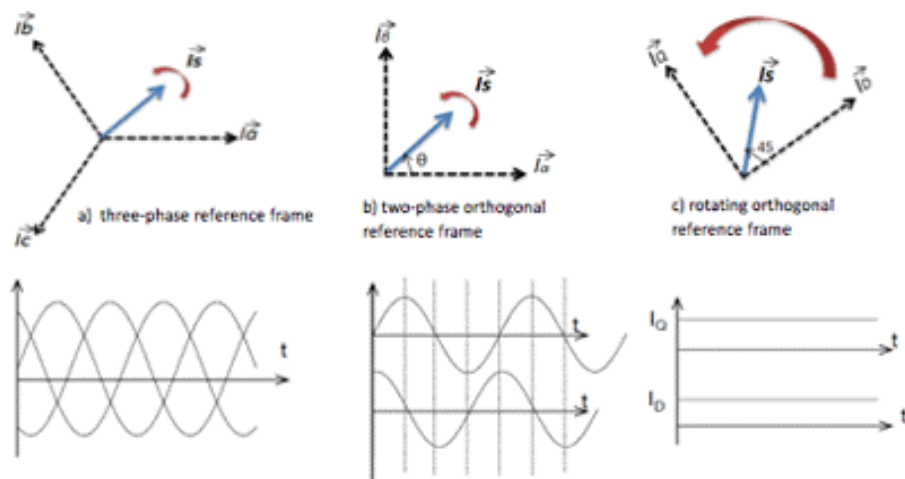


Fig. 22 –Field Oriented Control coordinates transformation.<sup>5</sup>

The transformation of the system currents with respect to three different reference systems is shown in Figure 22. Here a) is the three-phase AC system  $a, b, c$  fixed on the stator, b) represents the equivalent two-phase AC system  $\alpha, \beta$  fixed on the rotor, whereas c) is the equivalent two-phase DC system  $d-q$  rotating at the same speed of the.

<sup>5</sup> M. Sundaram, “Implementing field oriented control of a brushless DC motor”, 01 April 2012, [www.eetimes.com/document.asp?doc\\_id=1279321](http://www.eetimes.com/document.asp?doc_id=1279321).

The FOC aims to transform the  $a, b, c$  coordinates into  $d-q$  coordinates, passing through the  $\alpha, \beta$  coordinates, and viceversa, in order to express the magnetomotive force and the magnetic field of the rotor with respect to two orthogonal components, that are  $d$  and  $q$ , where  $d$  is the *direct axis* aligned with the flux and  $q$  is the *quadrature axis*. The  $d$  component gives information about the rotor position  $\theta$ , whereas  $q$  indicates the reference torque for the motor. These components are computed on-line by means of two transducers, one for the absorbed phase currents and the other for the computation of the exacted position of the rotor.

Referring the machine model to the rotating axes system  $d-q$  allows the equivalence with the DC motor with separate excitation. Therefore, the excitation flux is produced by the permanent magnets and the armature current is equivalent to the stator current on  $q$  axis.

The block model of the motor in  $d-q$  axes is similar to the DC motor one. It is composed by two  $R, L$  coupled circuits, which correspond to two current control loops where the two current references will be  $I_{ds}^* = 0$  and  $I_{qs}^*$  given by an external speed control loop. Since the quantities referred to the  $d-q$  axes are direct currents, two PI regulators are used for current regulation purpose, as shown in Figure 23. The current regulators give as outputs the direct and “in quadrature” voltages through the direct and inverse Clark’s transformation, whereas the FOC of the motor is handled through the direct and inverse Park’s transformation.

Under nominal condition, the three motor phase voltages can be computed from the following equations:

$$\begin{bmatrix} v_a \\ v_b \\ v_c \end{bmatrix} - \frac{d}{dt} \begin{bmatrix} \lambda_a \\ \lambda_b \\ \lambda_c \end{bmatrix} = \begin{bmatrix} R_a & 0 & 0 \\ 0 & R_b & 0 \\ 0 & 0 & R_c \end{bmatrix} \begin{bmatrix} i_a \\ i_b \\ i_c \end{bmatrix} + \frac{d}{dt} \left( \begin{bmatrix} L_{aa} & L_{ab} & L_{ac} \\ L_{ba} & L_{bb} & L_{bc} \\ L_{ca} & L_{cb} & L_{cc} \end{bmatrix} \begin{bmatrix} i_a \\ i_b \\ i_c \end{bmatrix} \right)$$

where the three phase voltages  $v_{a,b,c}$  are function of the vector of the digital control signal for each of the three commutation poles, i.e.  $\mathbf{q} = [q_1 \quad q_2 \quad q_3]^T$ ,  $R_i$  and  $L_i$  are the electric resistance and inductance for the  $i$ -th phase and  $\lambda_i$  the concatenated flux.

Once obtained the sinusoidal voltages for the three phases, three currents at  $120^\circ$  are generated on the three sinusoidal phases, as shown in the following equations:

$$\begin{cases} i_a = i \sin(\alpha + 90^\circ) \\ i_b = i \sin(\alpha + 90^\circ + 120^\circ) \\ i_c = i \sin(\alpha + 90^\circ + 240^\circ) \end{cases}$$

These currents will be able to create a magnetic field at  $90^\circ$  with respect to the rotor, which intensity is proportional to the torque to be generated. Therefore, one can say that rotor position gave by the resolver determines the rotation of the rotating magnetic field, modulating the current in order to obtain a rotation of the magnetic field at a frequency that corresponds to the desired speed of the motor.

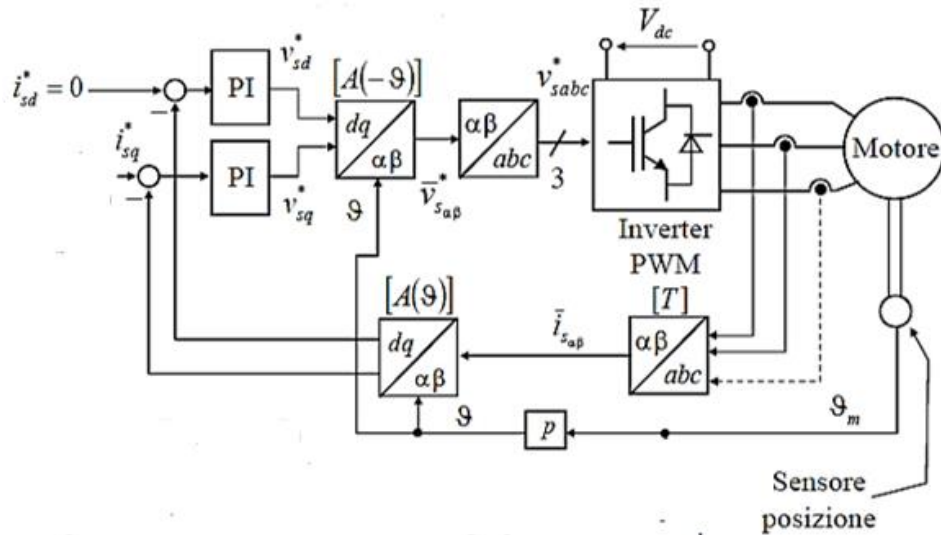


Fig. 23 – Field Oriented Control block diagram.

The motor electric circuit is connected to the inverter, which feeds the motor with the desired speed through a modulating signal for each of the six transistors (Tr) connected by two H-bridges, using the Pulse-Width Modulation (PWM) technique. This technique allows to generate an ON/OFF digital signal through the comparison of two signals, namely the *carrier* and the *modulate* signals, generated by the opening/closing of the transistors. Thus, the PWM technique permits to obtain an AC varying signal through a DC control logic.

Then, the *resolver* is a rotary transformer consisting of a stator and a rotor attached to the AC motor shaft. The primary winding of the stator is connected to a high frequency

sinusoidal signal, which is transmitted to rotor winding (called *Reference winding*). The pulsating magnetic field of the reference winding induces an alternating voltage in the measuring windings of the stator, namely *sine* and *cosine* windings. The relative amplitudes of the signal on the stator windings, which are orthogonal, completely describes the angular position of the rotor with respect to the stator (Fig. 24).

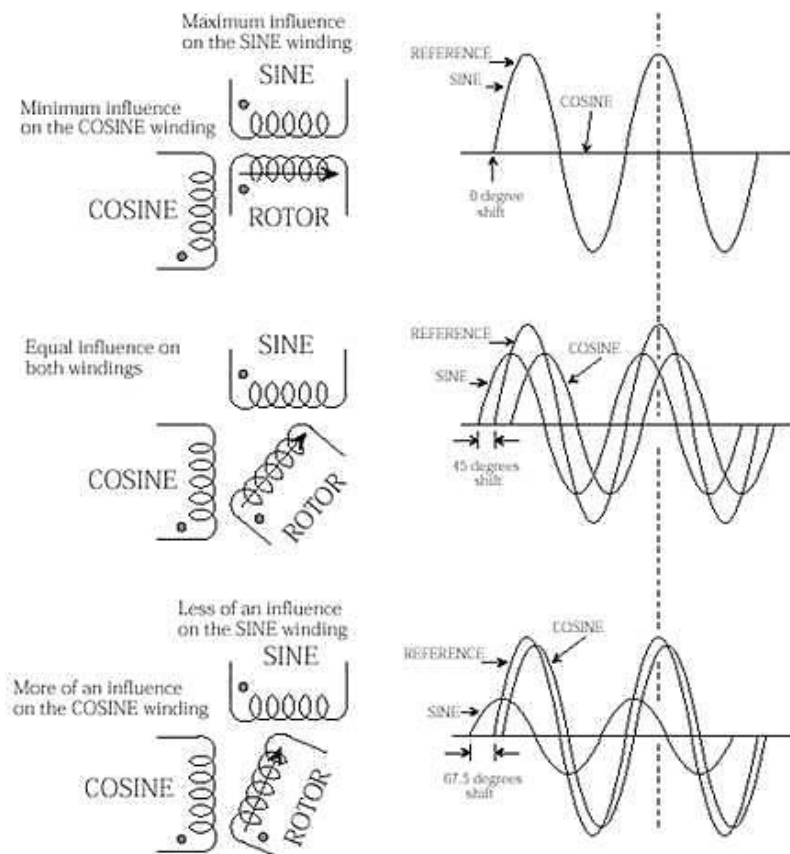


Fig. 24 – Resolver working principle. <sup>6</sup>

<sup>6</sup> Encoders and Resolvers: [www.automationprimer.com/2012/07/15/encoders-and-resolvers](http://www.automationprimer.com/2012/07/15/encoders-and-resolvers).

## 4.2.2 Mechanical Transmission

The electric motor is connected to a first pulley, which transmits the motion to a toothed belt transmission with a unitary transmission rate. Then, a second pulley is coupled to the nut of the linear actuator, in order to provide the torque to the screw-nut drive system. The satellite roller-screw SKF actuator transforms the rotary motion coming from the belt transmission into linear motion. This transmission is composed by four parts: the *nut* internally threaded in a complementary way with respect to the screw, which is the first part of the transmission coupled with the belt transmission; the *satellite rollers* with a rounded thread; the *cage*, which allows keeping the relative position between the satellite rollers. An *anti-rotation device* is coupled with the rod end in order to guarantee the proper transmission of the load between the mechanism and the rod. Thus, it allows the actual screw pitch at each nut rotation and, consequently, the correct linear position.

The target data of the satellite roller-screw SKF actuator are shown in Tab. 3.

**Tab. 3** – Rated data of the satellite roller screw SKF actuator.

<b>Data</b>	<b>Value</b>	<b>UoM</b>
Number of threads	4	-
Screw diameter	21	mm
Screw pitch	5	mm
Helix angle	4.33	°
Rollers number	9	-
Dynamic load	50.55	kN
Static load	81.97	kN
Axial gap	0.02	mm
Nut mass	0.4	kg
Screw mass/meter	2.7	kg/m
Nut inertia	141.2	Kgmm <sup>2</sup>
Rollers inertia	6.5	Kgmm <sup>2</sup>

# Chapter V

## Vibration Signals as Function of Static Airgap Eccentricity in EM

In general, diagnosis and monitoring of the system conditions require the collection and the analysis of specific data, containing precise information about incipient faults, malfunctions, etc.

Considering the case of electric motors, two of the main aspects that can be considered to detect the possible fault root cause are electrical causes (e.g. currents and voltages asymmetry) and mechanical causes (e.g. vibrations).

Vibrations detection is widely used to index faults in rotating machines. The vibration phenomenon occurs when the equilibrium conditions of the system are perturbed by imposing, for example, unbalanced initial conditions.

Supposing that the motor shaft is *rigid*, that is, a shaft whose first critical speed is higher than the motor operating speed, the deformability of the rotor can be neglected and vibrations can be measured near bearings supports. Here, the main dynamic loads and forces are applied, thus the vibrations can indicate the presence of forces generated by rotor unbalanced motion due to non-uniform airgap length (static or dynamic eccentricity). However, this also involves electrical anomalies related to an asymmetric magnetic flux distribution in the airgap. It must be said that, a simple analysis of the global vibration of the system is not enough for diagnostic purposes. Therefore, the frequency analysis techniques, such as the Fast Fourier Transform FFT analysis, are used to precisely highlight the parts of the signal spectrum, which are indicative of a specific malfunction [8].

## 5.1 Eccentricity in electric motors

As already mentioned in the previous chapter, several mechanical stresses bear upon key components of the electric motor. For example, an airgap eccentricity caused by the shaft misalignment or the bearings wear, causes an increase of these stresses during the motor operating cycle and can lead to stator vibrations.

First, the symmetric conditions between rotor and stator, that is, when their rotation axes rotate with precise concentricity, are analysed here.

The radial component of the Maxwell tensor, which represents the force per surface unit that enclose the airgap between two electromagnetic blocks, can be expressed in terms of magnetic induction  $B(T)$ :

$$\sigma_n = \frac{F_n}{S} = \frac{B^2}{2\mu_0}$$

where  $\mu_0$  is the vacuum magnetic permeability [ $H/m$ ].

In electric motors, these forces are orthogonal and symmetric with respect to rotor and stator surfaces. Therefore, when the rotor and the stator are concentric, the resultant of these forces is equal to zero.

Moreover, the magnetic flux in the airgap  $\Phi$  depends on the interaction between rotor and stator magnetomotive forces  $\mathcal{M}$  and it is proportional to the magnetomotive force itself:

$$\Phi = \frac{\mathcal{M}}{\mathcal{R}}$$

where  $\mathcal{R}$  is the reluctance of the magnetic circuit crossed by the flux.

Since the airgap reluctance is higher than the iron core one, it is possible in first approximation to neglect the latter for the magnetomotive force computation:

$$\mathcal{R} \cong \mathcal{R}_{airgap} = \frac{2\delta}{\mu_0 S}$$

Therefore:

$$\mathcal{M} = \Phi \cdot \mathcal{R} = B \cdot S \cdot \frac{2\delta}{\mu_0 S} = \frac{B \cdot 2\delta}{\mu_0}$$

where  $S$  is a normal surface crossed by the flux [ $\text{m}^2$ ] and  $\delta$  is the airgap length [ $\text{m}$ ].

The first harmonic component of the magnetomotive force has a sinusoidal distribution along the airgap: its period depends on the number of pole pair  $p_p$  and its amplitude is a sinusoidal which depends on the power frequency  $f$ :

$$\mathcal{M}_1(\beta, t) = \bar{\mathcal{M}}_1 \cos(\omega t - p_p \beta)$$

where  $\beta = \frac{z}{R}$  and  $\omega = 2\pi f$ .

Consequently, also the amplitude of the magnetic field first harmonic component is a sinusoidal:

$$B(\beta, t) = \frac{\mu_0 \bar{\mathcal{M}}_1}{2\delta} \cos(\omega t - p_p \beta) = \bar{B} \cos(\omega t - p_p \beta)$$

and, knowing that the radial component of the Maxwell tensor depends on the square of  $B$ , the following expression is obtained for the magnetic field:

$$B^2(\beta, t) = \frac{1}{2} \bar{B}^2 \cos(2\omega t - 2p_p \beta) + \frac{1}{2} \bar{B}^2$$

Hence, the radial force due to the Maxwell tensor has a sinusoidal component varying in time with a frequency that is twice the power frequency  $f$ .

Then, integrating the Maxwell strain along the airgap when the rotor and the stator are concentric, the resultant is equal to zero in all directions:

$$F_x = \int_0^{2\pi} \left( \frac{B^2(\beta, t)}{2\mu_0} \cos\beta \right) d\beta = 0$$

$$F_y = \int_0^{2\pi} \left( \frac{B^2(\beta, t)}{2\mu_0} \sin\beta \right) d\beta = 0$$

A different thing happens when the rotor and the stator are not concentric: the airgap length is no longer equal, i.e. varies with the rotor angle, and thus the Maxwell strain returns non-zero resultants.

This phenomenon is called *eccentricity* and it is a common fault that can occur even before the electric machine installation, like during the manufacturing process or shipping. Moreover, inappropriate assembling, bent rotor shafts, coupling misalignment and unbalanced load can cause rotor eccentricity. In fact, the latter may lead to problems such as unbalanced magnetic pull, vibration, noise and torque pulsations.

Airgap eccentricity can appear in the form of *static* or *dynamic* eccentricity. In the case of static eccentricity, a rotor rotates over its own axis; hence, the minimum air-gap position is fixed in space and time. Besides, integrating the radial component of Maxwell tensor along the airgap length, a non-zero resultant is obtained in the minimum airgap length direction. The static eccentricity also produces an additional radial component, which is a sinusoid with twice the power frequency.

$$\delta(\beta) = \bar{\delta} + E \cdot \cos(\beta)$$

where  $\bar{\delta}$  is the airgap between stator and rotor without misalignment. The second term represents the variation of the air gap with  $\beta$  (i.e. a generic position taken with respect to stator reference system) related to the misalignment  $E$ , as shown in the Figure 25.

Dynamic eccentricity occurs when the rotor centre does not coincide with the centre of rotation, and so the minimum airgap revolves with the rotor. This means that dynamic eccentricity is a function of space and time. Furthermore, it produces a mechanical unbalance in the form of a centrifugal force rotating at rotor speed, which leads to vibration at the same frequency [9]. The dynamic eccentricity also produces an additional magnetic force, rotating with rotor speed  $\Omega$ , to the one produced by the mechanical unbalance.

$$\delta(\beta, t) = \bar{\delta} + E \cdot \cos(\beta - \Omega t)$$

where  $\bar{\delta}$  is the airgap between stator and rotor (without misalignment). In this case, the second term represents the variation of the air gap with  $\beta$  and  $t$  related to the misalignment  $E$ . Therefore, stator or rotor magnetic field unbalances can cause non-sinusoidal induction distribution  $B$  and effects on vibrations.

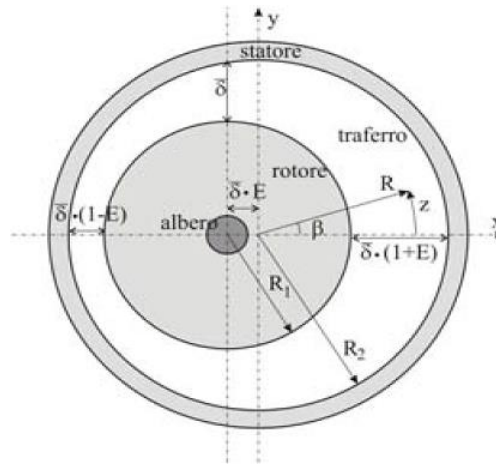


Fig. 25 – Rotor eccentricity representation

It must be noted that static eccentricity variations result in the introduction of vibration and dynamic eccentricity components in the motor current. This indicates that dynamic eccentricity is a by-product of static eccentricity, as it will be shown later. Therefore, in most cases, static and dynamic eccentricities simultaneously occur and therefore mixed eccentricity must be considered. In that case, the stator centre, the rotor one and the rotation axis are displaced with respect to each other. In Figure 26 the three types of eccentricity are represented.

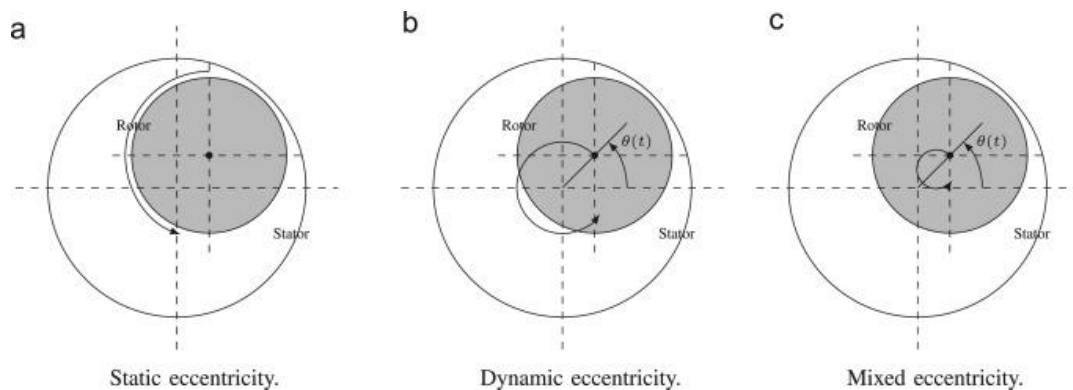


Fig. 26 - Representation of static (a), dynamic (b) and mixed (c) eccentricities, for revolving rotor (black arrow).<sup>7</sup>

<sup>7</sup> E.Elbourchikha, V.Choqueuseb, M.Benbouzid, "Induction machine bearing faults detection based on a multi-dimensional MUSIC algorithm and maximum likelihood estimation, ISA Transaction, Volume 63, July 2016, Pages 413-424.

### 5.2 Detection of rotor eccentricity in EM

Rotor movements in electric induction motors are the result of electromagnetic interaction between the airgap fluxes produced by the three-phase stator windings and induced rotor currents. In fact, in the case of static eccentricity fault, for example, the motor that has more than one polar couple generates a periodically variable magnetic flux, since the air gap varies during its  $360^\circ$  degrees turn. Radial magnetic forces are generated in the airgap between the rotor and stator surfaces and are proportional to the flux density squared. These forces lead to winding and stator core vibration. As faults associated with rotor and stator windings and airgap variations alter the normal airgap flux waveform, quantities that are functions of the airgap flux will also change. This means that stator core vibration, line current and stray flux signals can be used to monitor the condition of the BLAC motor.

Another consequence of this phenomenon is the non-uniform distribution of magnetic field and flux in the air gap, which affects the phase back electromotive force waveforms and, consequently, increases electromagnetic torque ripples caused by eccentricity.

In addition, eccentricity causes a pulling force on the rotor that tries to drive it even further from the stator bore centre. In the case of static eccentricity, this is a steady pull in one direction, generating an unbalanced magnetic pull (UMP). Instead, dynamic eccentricity produces an UMP, which acts on the rotor and rotates at rotor rotational velocity. Both types of eccentricity cause excessive stressing of the machine and greatly increase bearing wear. This is also feasible for a rotor-to-stator rub to occur with consequential damage to the core and windings and the rotor cage. As shown in [9], the static and dynamic eccentricities significantly modify the back-EMF and torque waveforms of rotational asymmetric machines. The static eccentricity does not affect the harmonic contents of back-EMF, but results in unbalanced three phase back-EMFs.

It is well known that there will be an inherent level of static airgap eccentricity in three-phase induction motors due to manufacturing and assembly methods. In practice, this means that when dynamic eccentricity occurs, then both types of eccentricity exist together.

As already explained, when eccentricity occurs, the airgap field consisting of the fundamental component of rotor and stator magnetomotive force harmonics and slot permeances will have additional harmonic components due to the fault. Meanwhile, the degree of the fundamental harmonic and ripples vary with the type and eccentricity degree. In [10] it is showed that there is a particular frequency component within the airgap flux density waveform, which depends on the position and number of rotor slots as follows

$$f_{ecc(n_d)} = \left[ (kR \pm n_d) \left( \frac{1-s}{p} \right) + \eta \right] f_s \quad (2)$$

where  $f_{ecc(n_d)}$  is the frequency component due to the principle slot harmonic (PSH). The eccentricity order is  $n_d = 0$  in case of static eccentricity and  $n_d = 1, 2, 3, \dots$  in case of dynamic eccentricity,  $f_s$  is the fundamental supply frequency,  $R$  is the number of rotor slots,  $s$  is the slip,  $p$  is the number of pole pairs,  $k$  is any integer, and  $\eta = \pm 1, \pm 3, \pm 5, \dots$  is the order of the stator time harmonics that are present in the power supply driving the motor. If these harmonics are a multiple of three, they may not theoretically be present in the line current of a balanced three-phase motor.

When both static and dynamic eccentricity are present, that is, mixed eccentricity, additional frequency components given by

$$f_{mixecc} = f_s \pm k f_r, \quad k = 1, 2, 3, \dots$$

will be present in the stator current spectrum of any three-phase induction machine irrespective of  $p$  and  $R$ , where  $f_r$  is the rotational frequency of the machine obtained by the following equation, with two poles pair  $p$  and considering an ideal condition with zero slip coefficient  $s$ :

$$f_r = \left( \frac{1-s}{p} \right) f_s$$

However, these additional frequency components will lead to other additional current spectra peaks at the same frequencies described by (2) for static or dynamic eccentricity related components.

For rotational asymmetric machines, both types of eccentricities may affect the electromagnetic performance, but in different ways as reported in [11] and following explained.

- **Static Eccentricity**

The static eccentricity does not affect the harmonic contents of the back-EMF, but only changes the harmonic magnitude. Whether the harmonic magnitude is increased or reduced, it depends on the winding location, i.e. the phase facing the smaller airgap has larger back-EMF. The unbalanced three phase back-EMFs can be decomposed into two sets of balanced back-EMFs, one being forward rotating and the other backward rotating. The main torque ripple component due to the static eccentricity is  $(2p)th$ , which is mainly from the interaction between the  $(p)th$  order current and  $(-p)th$  order back-EMF.

- **Dynamic Eccentricity**

The dynamic eccentricity enriches the harmonic contents of the flux linkage and back-EMF. The flux linkage and phase back-EMF components due to the rotating eccentricity are the  $(np \pm 1)th$  temporal order harmonics. The line back-EMF components due to the rotating eccentricity can rotate forward and backward. These harmonics components of phase back-EMF are the triple harmonics, which cannot be seen from the line back-EMF.

In this Thesis, the distortions in harmonics of the phase currents due to the static eccentricity in rotational asymmetric machines will be investigated. Since motor torque is the result of the interaction between motor back-EMFs and phase currents, back-EMFs distortion can affect motor electromagnetic torque ripples, as well as phase currents distortion.

# Chapter VI

## Linear Model of the EMA

In order to characterize the behaviour of the whole servosystem, the development of a mathematical model is fundamental. In this Chapter, a linear model for the Electromechanical Actuator (EMA) is considered, carried out through the characteristic equations of each components. The model considered is schematically illustrated in the block diagram in Figure 27. Starting from the well-known physical equations of dynamics and electromagnetism, the servosystem has been modelled analytically, employing a lumped parameter representation of the components. Although the linear model shown here represents a good approximation of the real system even in the presence of nonlinearities, it will not be used for the simulation activities. It is outlined mainly to describe in a clear way how the model works, especially with the aim of an its possible integration with the MPC controller in a second stage. However, a high-fidelity non-linear representation of the considered EMA will be employed for these purposes, since it accounts for several aspects of the actuator operations from a physical point of view, included non-linearities due to saturations and filters.

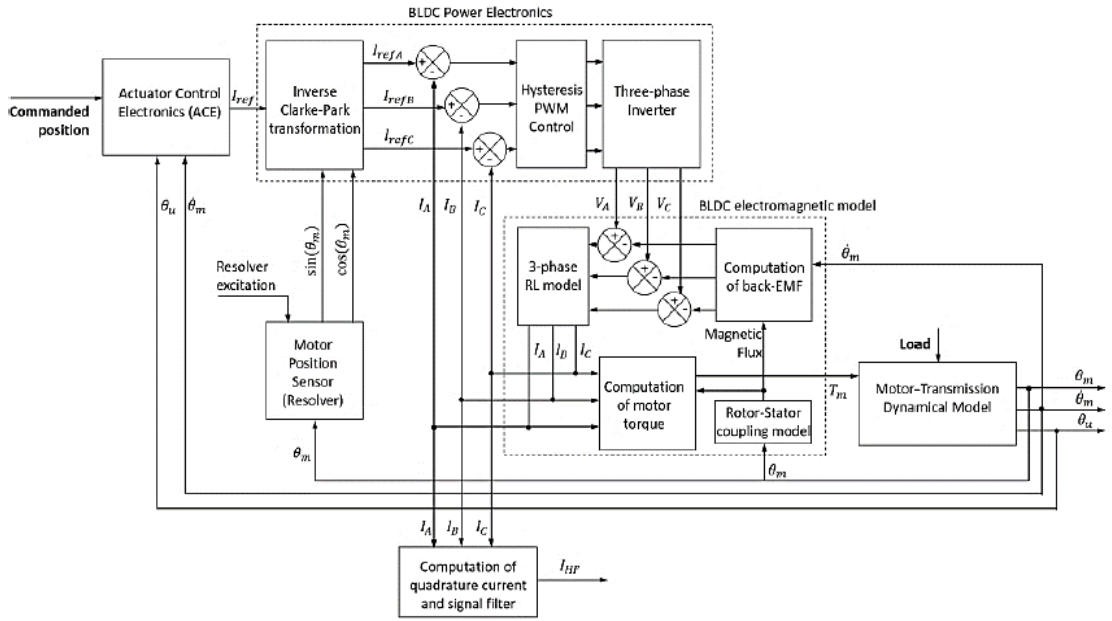


Fig. 27 – High fidelity block diagram of EMA model

## 6.1 EMA model

### 6.1.1 Electric model

The electric motor is a sinusoidal AC brushless with permanent magnets, but from a practical point of view, it can be seen as a DC motor for an easier modelling without great loss of accuracy. Under these hypotheses, Kirchhoff's law and torque equation can be considered for modelling the motor:

$$V_A = Ri + L \frac{di}{dt} + k_e \omega \Rightarrow \bar{i} = \frac{1}{(Ls + R)} (V_A - k_e \bar{\omega})$$

$$T_m = k_t \cdot i$$

where  $V_A$  is the armature voltage,  $i$  is the armature current,  $R$  is the electric resistance,  $L$  is the inductance,  $\omega$  is the rotor's angular speed,  $T_m$  is the torque generated by the motor current and  $k_e$  and  $k_t$  are respectively the voltage and the torque constants.

### 6.1.2 Mechanical transmission

A belt transmission and two pulleys with equal radius, which thus transmits the rotary motion with unitary transmission rate to a screw-nut drive system, compose the mechanical transmission of the system. The screw-nut system will convert the rotary motion into the linear one thanks to a SKF roller screw.

The efficiency of the belt reducer is:

$$\eta_t = \frac{T_m \dot{\vartheta}_m}{T_l \dot{\vartheta}_l}$$

where  $T_m$  and  $T_l$  are the electromechanical torque and the load torque, respectively, while

$$\tau_t = \frac{\dot{\vartheta}_m}{\dot{\vartheta}_l}$$

is the transmission rate, which in this formulation is assumed as unitary.

Then, the motion is transmitted to the power screw where the external force  $F_{ext}$  is applied and produces the load torque acting as a disturbance. The *direct efficiency* is the efficiency of the planetary rollers in the SKF actuator when the rotating motor produces a translation:

$$\eta_v = \frac{F_{ext} p}{T_l 2\pi}$$

from which the load torque can be computed as:

$$T_l = F_{ext} \frac{p}{2\pi} \frac{1}{\eta_v}$$

where  $\frac{p}{2\pi}$  is the transmission ratio from rotating motion to linear motion. Therefore, once integrated the output speed from the roller screw and obtained the angular position, the linear position of the screw can be derived.

### 6.1.3 Equilibrium rotation equation of motor shaft

Since the servosystem has a parallel interface, the equilibrium equation for each axis can be written using the total inertia computed with respect to the motor shaft.

For the first shaft, the equation is:

$$T_m - T_1 = J_1 \frac{d\omega_1}{dt}$$

and for the second one:

$$T_2 - T_3 = J_2 \frac{d\omega_2}{dt}$$

where  $J_1, J_2$  and  $\omega_1, \omega_2$  are the inertias and the angular speeds of the two shafts,  $T_m$  is the motor torque,  $T_1, T_2, T_3$  are the torque applied on the first shaft, on the second shaft and on the SKF roller-screw respectively.

For the sake of completeness, see the Appendix A for the full computation of the total inertia used in the rotation equilibrium equation.

## 6.2 Control Modelling

The control system of the EMA consists in three nested loops with the respective regulators, corresponding to current, speed and position control. They present the regulation dynamics, which grows from the outer to the inner loop, taking into account also the time constants of the system.

All the three loops regulators are of PI (Proportional-Integrative) types and consequently the transfer functions of all control loops are equal to each other, as shown below.

- **Position Control**

Here the linear position reference  $x_{rif}$  is compared with the position of the power screw measured through the resolver, which produces an error  $e_x$  that will be mitigated by the PI regulator. It generates a new reference for the linear speed  $\dot{x}_{rif}$ .

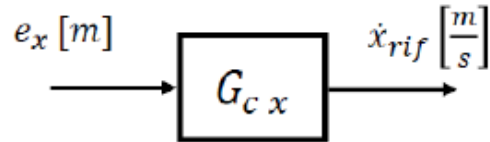


**Fig. 28** – Position Control Loop block

$$G_a = \left( \frac{k_{p_x}}{k_{i_x}} s + 1 \right) \frac{k_{i_x}}{s}$$

where  $k_{p_x}: \left[ \frac{rad}{m} \right]$ ,  $k_{i_x}: \left[ \frac{rad}{m \cdot s} \right]$

- **Speed Control**

The rotational speed reference  $\dot{\theta}_{rif}$  is compared with the speed of the load computed through the resolver producing an error that will be passed to the PI regulator. It generates a new torque reference  $C_{rif}$  that summed to the torque feedforward makes easier to predict the torque reference and speed up the system response.

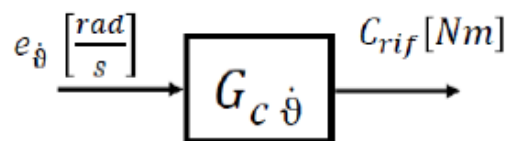


**Fig. 29** – Speed Control Loop block

$$G_{c\dot{\theta}} = \left( \frac{k_{p\dot{\theta}}}{k_{i\dot{\theta}}} s + 1 \right) \frac{k_{i\dot{\theta}}}{s}$$

where  $k_{p\dot{\theta}}: \left[ \frac{Nm}{\frac{rad}{s}} \right]$ ,  $k_{i\dot{\theta}}: \left[ \frac{Nm \cdot s}{\frac{rad}{s}} \right]$

• **Current Control**

Since the motor is controlled through Field Oriented Control (FOC) in d-q axes, the speed reference coming from the outer loop and the feedback load speed are compared, producing the reference current  $i_q^*$  that is proportional to the torque. Instead, the reference for the current  $i_d^*$  is keep to zero, since it does not contribute to the motor torque because the motor has permanent magnets.

Therefore, the two current references enter in the PI regulators, generating as outputs the voltage references  $u_{d'}^*$  and  $u_{q'}^*$  that will be passed to the PWM in order to switch the inverter.

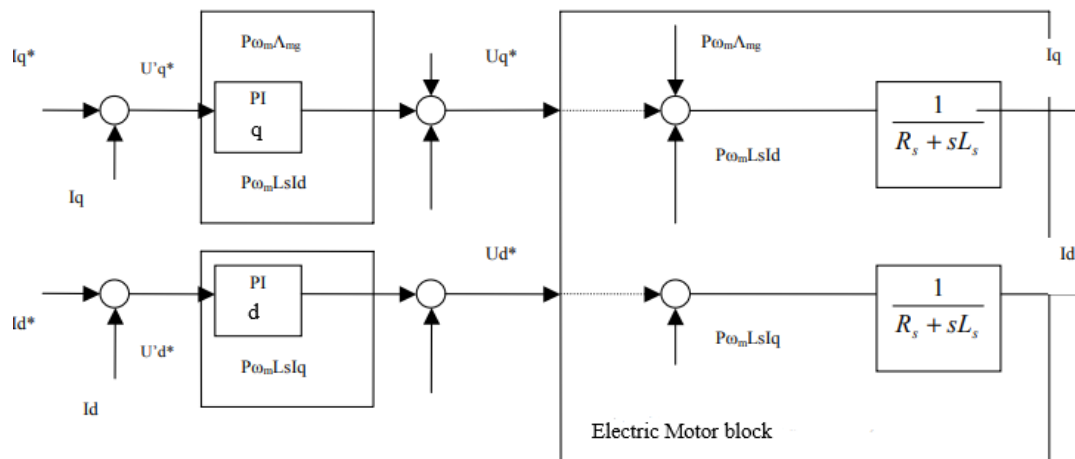


**Fig. 30** – Current Control Loop using FOC

## Linear Model of the EMA

The two control loops are not independent, but they influence each other because of the coupling between d-q axes and due to the presence of the term  $p\omega L_s i_q$  and the magnetic flux  $p\omega_m \Lambda_{mg}$ . If the inverter constant time  $\tau_c$  is sufficiently small with respect to the other system constants, it is possible to neglect the coupling between the axes inserting another coupling, similar to the intrinsic one of the motor (*decoupling*).

The decoupling between the two loops is obtained subtracting from  $u_{d'}^*$  the magnetic flux and adding the same term to  $u_{q'}^*$ . The quantities added to the references compensate the ones that are yet in the motor, obtaining a greater simplification of the block schemes.

Thus, the two decoupled and simplified current loops will be the ones shown in Figure 31:

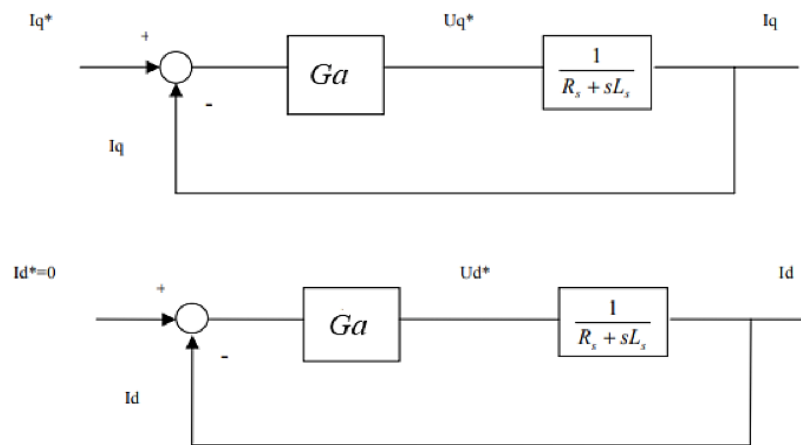


**Fig. 31** – Current Decoupled Control Loop block

and the transfer function is:

$$G_a = \left( \frac{k_{p_i}}{k_{i_i}} s + 1 \right) \frac{k_{i_i}}{s}$$

where  $k_{p_i}: \left[ \frac{V}{A} \right]$ ,  $k_{i_i}: \left[ \frac{Vs}{A} \right]$ .

In every control loops, inputs and outputs are coupled by the proportional coefficient  $k_p$ , which influences the output values. If increased, this parameter speeds up the transient reducing the error between the set signal and the feedback one, but there still exists an offset between the two signals. In fact, in order to have a null steady state error, the proportional gain contribution should have an infinite value since, while the error is reducing,  $k_p$  action is less intense. Therefore, an integral action is needed to eliminate, or at least reduce, the steady state error for constant references as fast as  $k_i$  is high.

The disadvantage deriving from an exclusive P control is the destabilization of the system, due to the increase of  $k_p$  parameter, and for what concern an exclusive I control the destabilization is due to the decrease of the integration time value  $\tau_i$ .

The frequency response of the Proportional-Integrative contribution is represented in Figure 32.

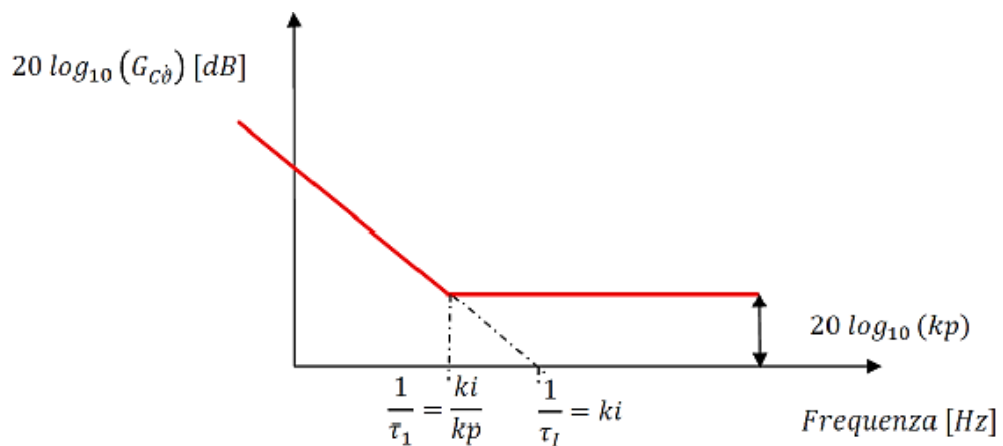


Fig. 32 - The frequency response of a Proportional-Integrative contribution

## 6.3 Simulink model of the servosystem

The primary goal of this work is the proposal of a technique able to identify symptoms related to the presence of a certain degree of eccentricity alerting that an EMA is

degrading. Therefore, a suitable simulation test environment is created and implemented in MATLAB/Simulink.

The physical model of the servosystem is described by the interconnection of two blocks, the one for the BLAC motor drive and the one representing the mechanical transmission, as shown in Figure 33. The latter is then connected to a block modelling the resolver, which provides the reading of the motor position and speed.

The BLAC drive block, together with the mechanical transmission and the resolver blocks, are comprehended in the speed loop control. The inputs constituted by the reference current and the DC voltage are then used by PWM and inverter, whereas the output are the phase currents, the motor position and the electromechanics torque. The torque enters in the mechanical transmission block in the form of external friction, together with the load torque produced by the external force  $F_{ext}$ . The mechanical transmission considers also the inertia and the friction values of the electric motor shaft, the pulleys and the power screw, and they all constitute a load for the EMA.

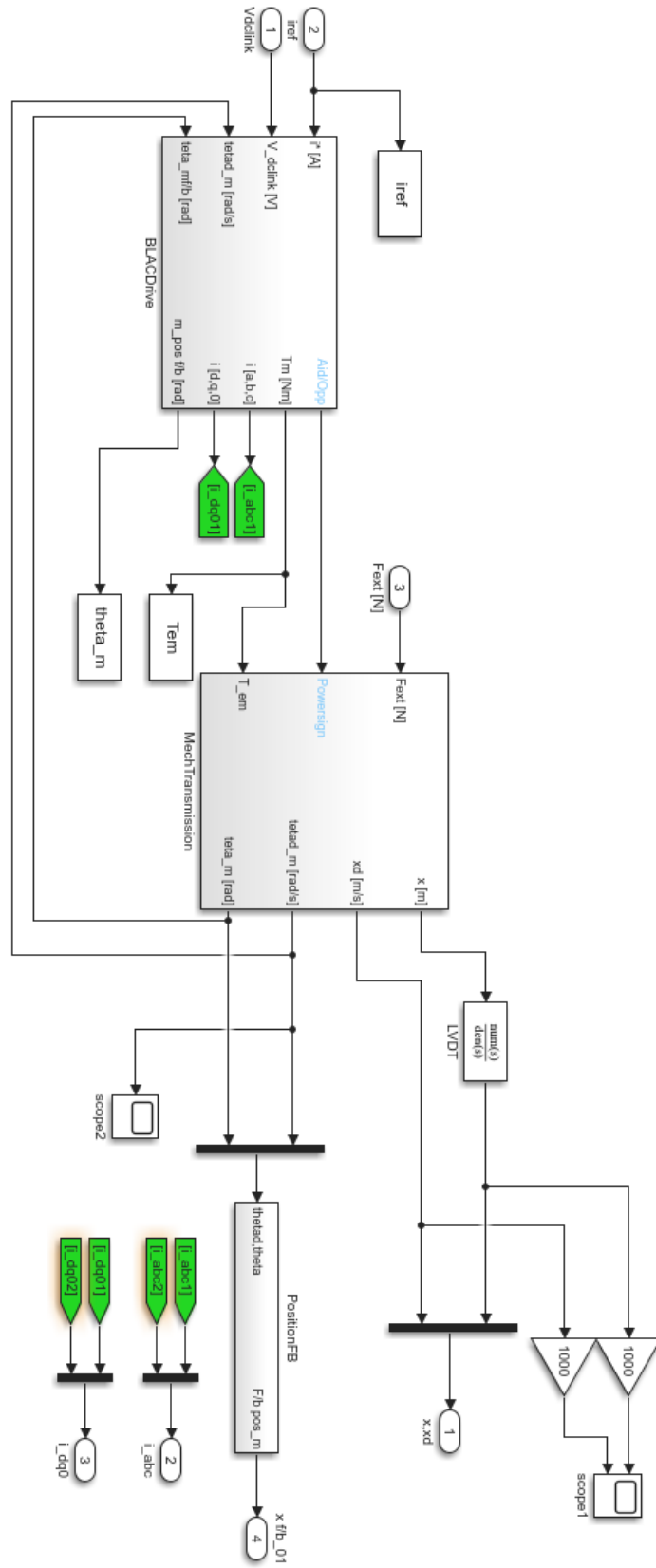


Fig. 33 – Simulink physical model

The dynamic model of the electric driver is composed by several interconnected functional subsystems: the electric power unit (EPU), the motor windings and the torque evaluation module. The EPU subsystem is used to simulate the control currents in d-q axis, the PWM modulation of the voltage signal and a functional model of the digital inverter. The other subsystems describe the electric motor dynamics for each phase, compute the electromagnetic torque and approximate the windings thermal behaviour. The d-q axis control features two PI regulators receiving as input the current command and the filtered current feedback from the motor subjected to Park transformation. The output of the second current controller is then transformed back to the three-phase system and used in a PWM modulator based on a triangular bipolar wave carrier that generates the vector of the digital control signal for each of the three commutation poles, namely  $\mathbf{q} = [q_1 \quad q_2 \quad q_3]^T$ .

Finally, the outer control loop is the position one, which receives as input a reference position signal, which must be correctly tracked by the feedback position coming from the load (i.e. conducted pulley + power screw). The full model for the system is shown in Figure 34.

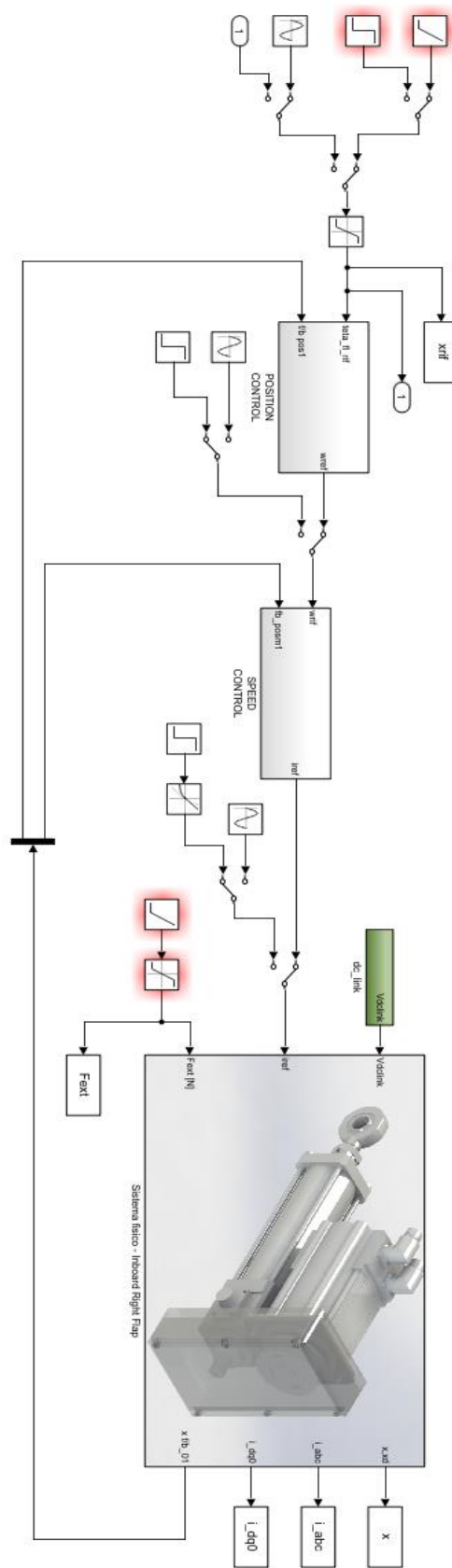


Fig. 34 – Physical block model with the control loops

## 6.4 Airgap-length variation block model

The static eccentricity equations seen in the Chapter 5.1 can be both expressed, for simplicity, through the following equation:

$$\delta(\theta) = \bar{\delta} [1 + E \cos(\theta - k\omega t)]$$

where  $\theta$  is the angular rotor position,  $\omega$  is the rotational speed,  $E = e/\bar{\delta}$  is the relative eccentricity, given by the ratio of the rotor displacement  $e$  and the nominal airgap length  $\bar{\delta}$ . The coefficient  $k$  indicates the type of eccentricity present in the motor; it is equal to 0 for the static eccentricity and 1 for the dynamic one. As already mentioned, the difference between healthy, static eccentricity and dynamic eccentricity cases is in the calculation of the airgap length.

In this context, the consequences of faults in servomechanism performances are studied, simulating their effects on the magnetic coupling between stator and rotor through angular modulations of the back-emf coefficients and their values. The purpose is to act on the three back-emf constants  $k_{ei}$  (one for each branch) modulating their sinusoidal reference values as a function of rotor eccentricity and, thus, of angular position and speed (in the case of dynamic eccentricity) [4], obtaining:

$$K_{ei} = k_{ei} \cdot \delta(\theta) = k_{ei} \bar{\delta} [1 + E \cos(\theta - k\omega t)], \quad i = a, b, c$$

The so obtained three constants are then used to calculate the back-emf induced on the corresponding stator windings and, therefore, to evaluate the mechanical torque contributions generated by the three motor phases.

In this Thesis, only the static eccentricity case is considered. Therefore, the equation for the voltage constant will be:

$$K_{ei} = k_{ei} \cdot \delta(\theta) = k_{ei} \bar{\delta} [1 + E \cos(\theta)], \quad i = a, b, c$$

The Figure 35 shows the Simulink model inserted in the back-emf computation block in order to realize the  $\delta$  variation.

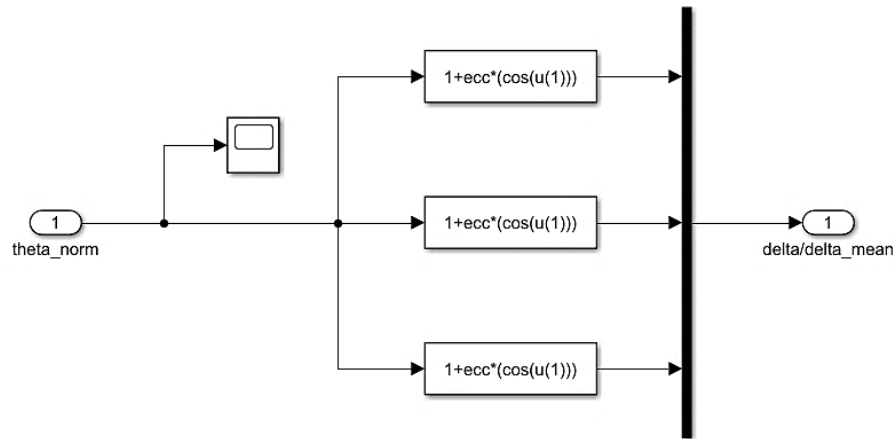


**Fig. 35** – Airgap variation block

It will be analysed in the next chapter that it is possible correlate the progressive static eccentricity with the instantaneous value of each current phase (used as failure precursors) by means of an algorithm called Fast Fourier Transform (FFT), based on the Fourier spectral analysis of motor phase currents.

# Chapter VII

## Simulation Activities Setting

The aim of this Chapter is to recreate the presence of the static eccentricity fault into the servo actuator and to observe the system behaviour under different conditions. This type of fault is linearly introduced until the system reaches a failure condition and fault data are recorded. In order to verify whether the system response is the one expected or not, several tests are conducted for healthy motor and faulty motor. They are performed under different percentage of the nominal load and rotor speed rate.

### 7.1 Preliminary system analysis

In this section, in order to explain the performance of the proposed numerical model, the motor response to a reference position is presented, in no-load and load conditions. The reference position command is a percentage of the actual input equal to  $x_{in} = 0.1 m$ , starting at  $t = 0.1 s$ , whereas the external load  $F = 1000 N$  is applied at  $t = 0.25 s$ . The value of eccentricity ratio introduced in the system to simulate the fault presence goes from 0 (no-eccentricity) to 0.3. Theoretically, for eccentricity values bigger than 0.3, the bearings wear becomes so severe that any attempt of maintenance will be useless. Moreover, beyond this value the system shows a saturated response that is not useful for the analysis purpose.

The working condition scenarios are summed in Tab.4:

Tab. 4 – System working conditions

Reference position $\theta$ [%]	External load $F_{ext}$ [N]
30	0
50	200
100	500

The length of the simulation is  $t = 1$  s. Here for simplicity only the results obtained with nominal reference position in no-load condition and in the “worst-case” condition, with the 50% of the external load and with the 30% of the nominal reference position. However, the system analysis in the remaining working condition shows similar results. As one can see from Figure 36, the back-emf  $e_a$  magnitude increases with growing eccentricity ratio as expected and shows a slight deformation on the lower and upper peaks. The same increase can be noticed in phase currents  $i_a$  and torque signals  $T$ , where also appears an asymmetry due to the eccentricity phenomenon (Fig. 37, 38). Moreover, the latter causes an instability of the system as well, consisting of an oscillating behaviour of the analysed signals around the steady-state condition. It should be mentioned that, since a realistic model of the EMA is involved in the study, the steady-state condition is not perfectly reached neither with SE equal to zero, due to intrinsic non-linearities of the considered model.

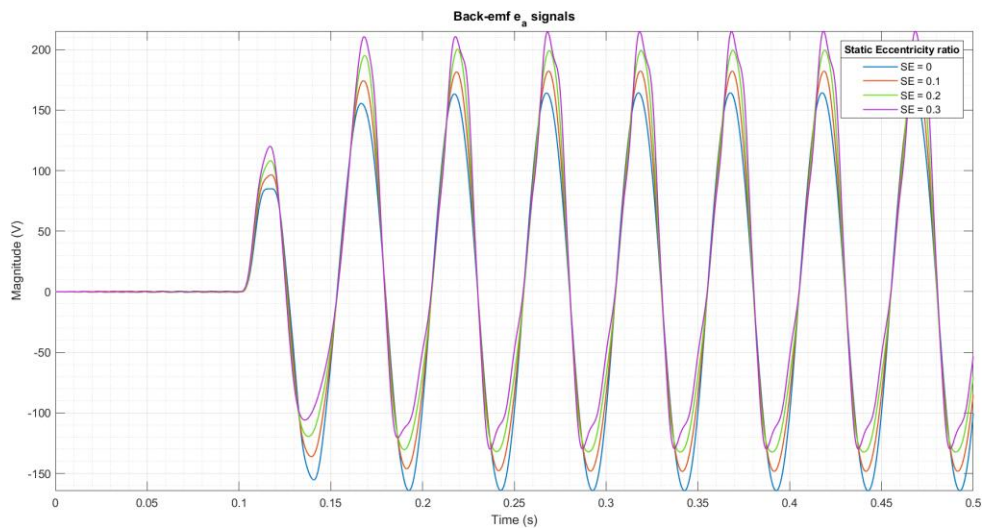
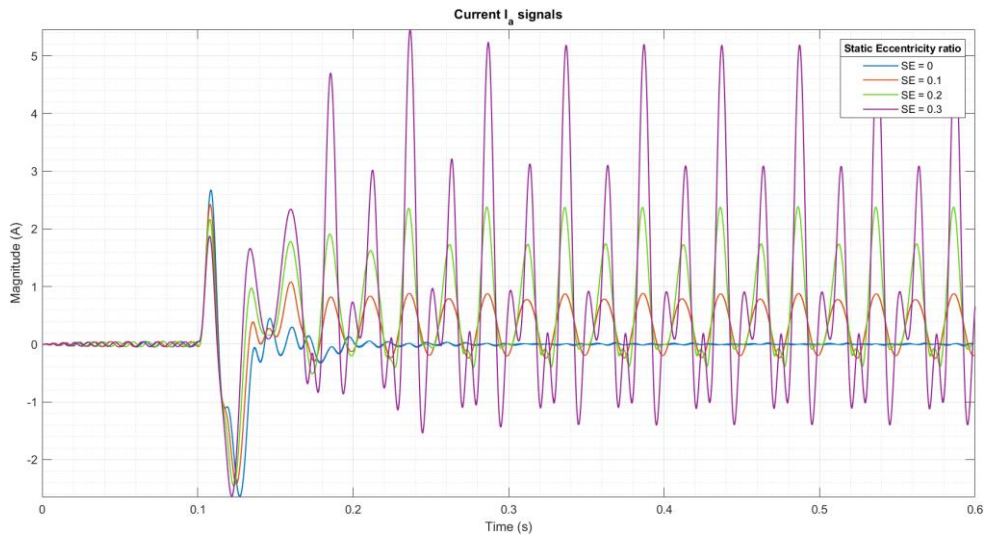
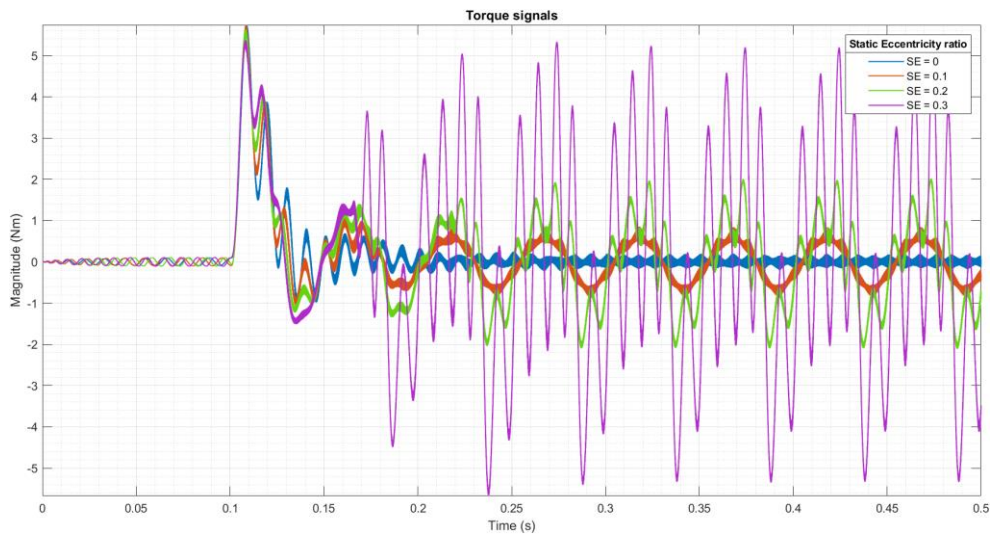


Fig. 36 – Back-emf  $e_a$  signals plot in no-load condition at nominal speed  $\omega_r$ .



**Fig. 37** – Current  $i_a$  signals plot in no-load condition at nominal speed  $\omega_r$ .



**Fig. 38** – Torque signals plot in no-load condition at nominal speed  $\omega_r$ .

A similar behaviour is registered with  $0.5F_{ext}$  and  $0.3\omega_r$ , for all the three considered parameters (Fig. 39, 40, 41). However, in this case the load  $F_{ext}$  introduction does not have a big impact on back-emf, such as on the current and, consequently, on the torque. In fact, the presence of an external load causes a distortion of the current signals that generates a sort of settling ramp in the torque signals, which is proportional to the load

value. For what concerns the rotor speed, a decrease in this parameter is reflected in an attenuation of the signals magnitude that is found in every considered parameter.

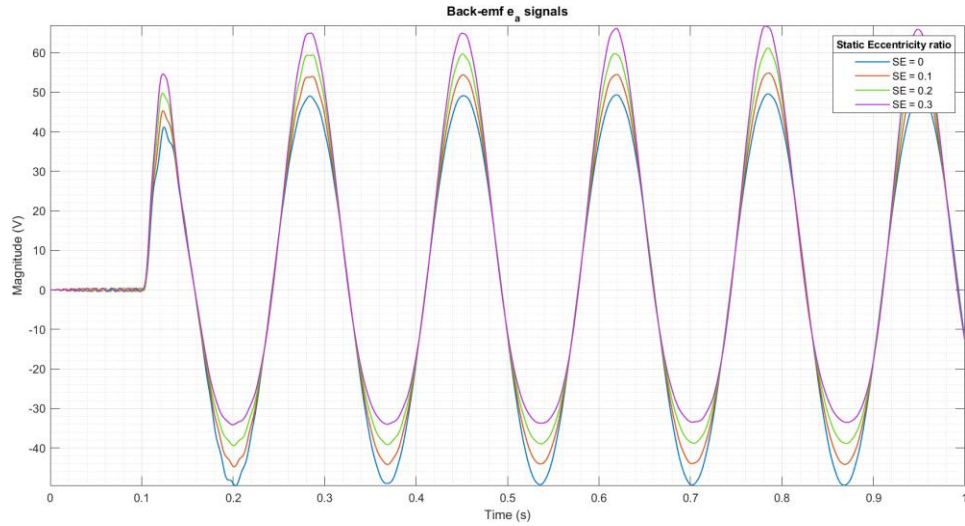


**Fig. 39** – Back-emf  $e_a$  signals plot with  $0.5F_{ext}$  and  $0.3\omega_r$ .

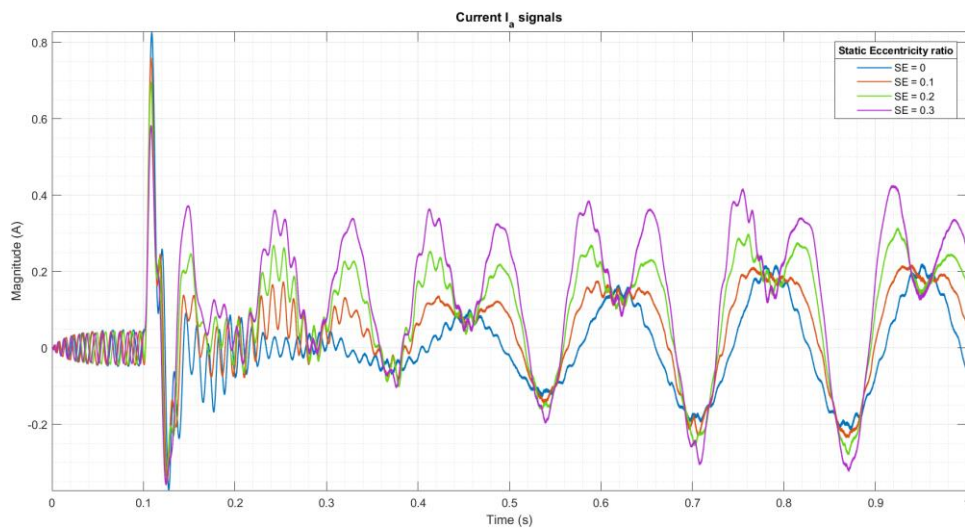


**Fig. 40** – Current  $i_a$  signals plot with  $0.5F_{ext}$  and  $0.3\omega_r$ .

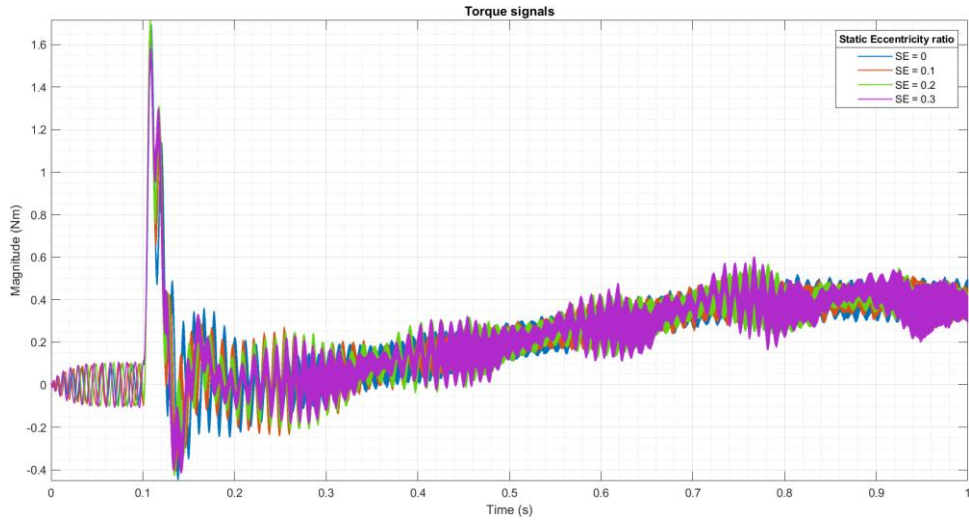


**Fig. 41** – Torque signals plot with  $0.5F_{ext}$  and  $0.3\omega_r$ .

The aim of the next paragraphs is to prove the correlation between the progressive static eccentricities with the phase currents used as failure precursors by means of an algorithm, based on the Fourier spectral analysis.

## 7.2 Motor Current Signature Analysis (MCSA) for fault detection

Currently, different non-invasive techniques are adopted for fault diagnosis of electrical machines, such as vibration analysis and Motor Current Signature Analysis (MCSA). This Thesis considers MCSA applied to the study of the rotor phase currents, and therefore, of back- electromotive forces on frequency domain. Each fault in the induction motors has associated certain additional frequencies used for diagnosis [12]. Fast Fourier Transform (FFT) technique localizes those frequencies in the spectra. Currents are considered periodic time functions; hence, Fourier series can represent them. By evaluating the associated sidebands of eccentricity, FFT is able to reveal the condition of the airgap.

## Simulation Activities Setting

---

The Fast Fourier Transform relates phase currents sampled in time to the same currents sampled in frequency. In signal processing, the FFT can reveal important characteristics of a signal, namely, its frequency components. The magnitude of the signal gives information about the strength of the frequency components relative to other components. The FFT is based on Fourier series and represents complicated but periodic functions as infinite sum of sine and cosine functions with different amplitude and phase. Here the Discrete Fourier Transform (DFT) is considered, since the analysed signals, defined by a vector  $X$  representing the phase current signal  $i_a$ , are known only at  $N$  uniform samples time during a finite time acquisition, thus obtaining a finite sequence data considering the signal periodic as:

$$Y_{k+1} = \sum_{j=0}^{N-1} e^{-i\frac{2\pi}{N}jk} X_{j+1}$$

where the exponential function represents one of  $N$  complex roots of unity where  $i$  is the imaginary unit. For  $X$  and  $Y$ , the indices  $j$  and  $k$  range from 0 to  $N - 1$ .

# Chapter VIII

## SE Fault Simulation and Diagnosis through Sidebands in FFT Analysis

An accurate fault diagnosis and static eccentricity (SE) detection can be realized when the healthy and faulty motors are compared under different loads and command inputs. Therefore, the use of the amplitude of the sideband components coming from the FFT analysis at frequencies  $f_s \pm kf_r$ , seen in Chapter 5.2, is the most reliable fault index, without taking the operating point into consideration. In fact, when eccentricity occurs, the airgap field consisting of the fundamental component, stator and rotor magnetomotive force harmonics and slot permeances will have additional harmonic components due to the fault. Furthermore, the degree of the fundamental harmonic and the ripples occurring at low-frequency range, vary with the eccentricity type and degree.

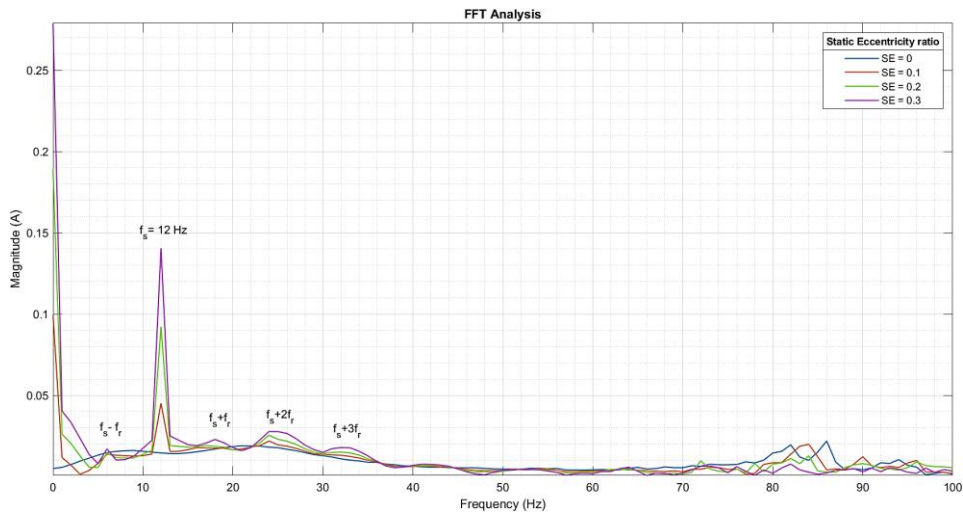
### 8.1 Diagnosis at no-load

Fig. 42 shows the frequency spectrum of phase current  $i_a$  for growing eccentricity ratio around the principal harmonic in no-load condition. The static eccentricity (SE) is applied to the model from 0% to 30%, with an increment of 10%. The principal harmonic ripple  $f_{PH}$  occurs at a frequency equal to the power frequency of the motor  $f_s$ , which depends on the position command given as input to the system model, and consequently, on the rotor nominal speed  $\omega_r$ . Therefore, the main ripple shifts according to the different speed rates considered. With the 100% of the nominal speed, the

principal harmonic appears at  $f_{PH} = 40 \text{ Hz}$ , whereas considering the 30% and the 50% it occurs respectively at  $f_{PH} = 12 \text{ Hz}$  and  $f_{PH} = 20 \text{ Hz}$  (fig. 43 and 44).

It can be observed that the amplitude of current peaks increase as the rotational speed of rotor increases. This can be explained considering the fact that the current is proportional to the back-emf, and, consequently, to the derivative of the rotor position given by  $\frac{d\theta}{dt} = \omega_r = 2\pi f_s$ , as seen in the airgap equation in Chapter 5.1 that is reported here for simplicity:

$$\delta(\theta) = \bar{\delta} [1 + E \cos(\theta)]$$



**Fig. 42** – FFT response of the current signal at  $0.3\omega_r$  in no-load condition.

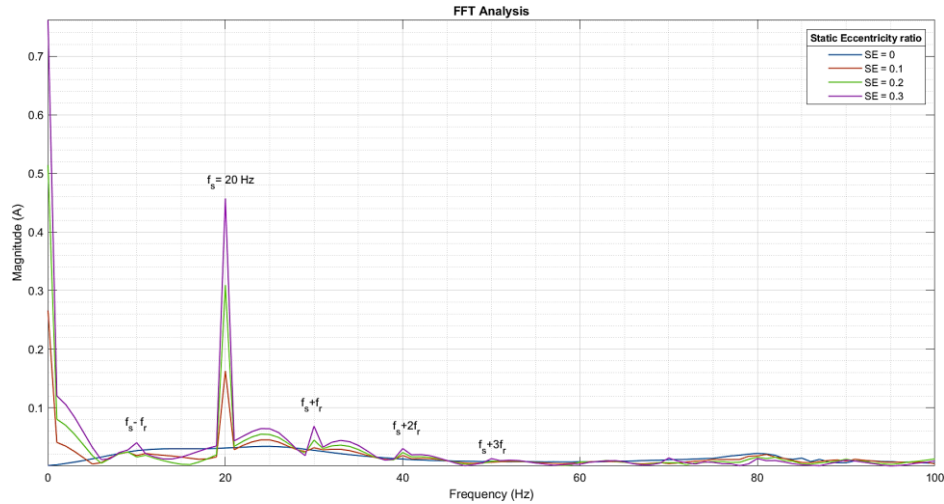


**Fig. 43** – FFT response of the current signal at  $0.5\omega_r$  in no-load condition.

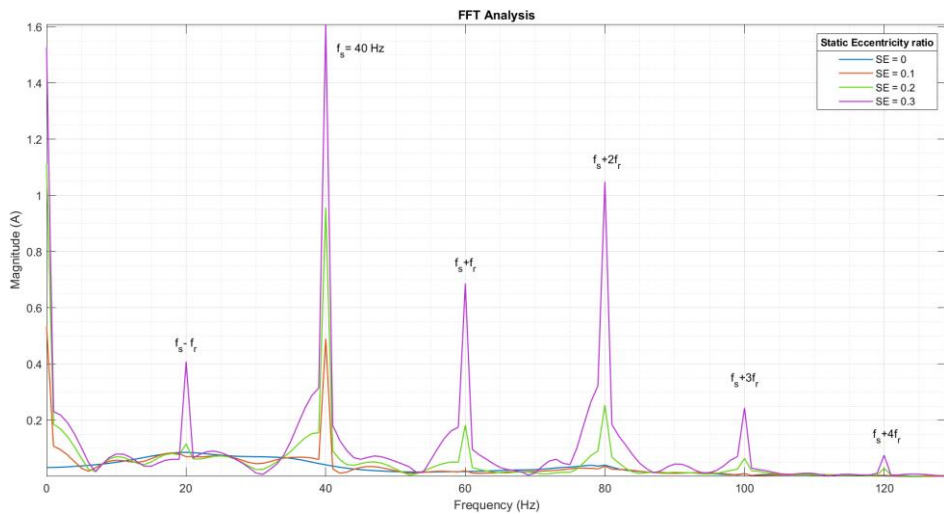


**Fig. 44** – FFT response of the current signal at  $\omega_r$  in no-load condition.

The figures show that, in all the three speed conditions, the static eccentricity causes the appearance of the sidebands at frequency  $f_s \pm kf_r$ , as expected. Due to the presence of the static eccentricity, the amplitude of the peaks increases with the eccentricity ratio. The presence of very high peaks at  $f = 0$  Hz is due to the fact that at  $t = 0$  s the current signal is not a perfect sinusoidal signal, but it is comparable to a DC signal, which gives this frequency response. In addition to this component, the sideband magnitude of  $f_s - 2f_r$  is added to the peak amplitude.

It must be also highlighted the presence of some noisy peaks around a frequency equal to  $2f_s \approx 80 \text{ Hz}$  that are most probably due to rotor speed. In fact, at that frequency value the system is settling to the reference value imposed by the outer control loops.

Generally, one can observe that the frequency response becomes weaker with the reduction of the rotor speed, with the sidebands due to the static eccentricity hid by other components due to a certain degree of noise of the system. This is because the model is a high-fidelity representation of a real servosystem, and thus it contains all the non-idealities that characterize a system of this type. On the other hand, with a rotor speed nearer to the nominal one, the sideband components are clearly distinguishable.

The tables reported in Annex B summarize the magnitude of frequency peaks from healthy to faulty motor with static eccentricity (SE) in no-load and loaded conditions shown in the next paragraph.

## 8.2 Diagnosis at different loads

### 8.2.1 Diagnosis at $F = 200 \text{ N}$

Figures 45, 46, 47 show the phase current frequency spectra for motor with increasing static eccentricity ratio with an external load equal to  $F = 200 \text{ N}$ . The corresponding simulation results show that the amplitudes of the harmonic components  $f_s \pm kf_r$  increase due to the increase in the load. The same consideration about the peaks behaviour done in the previous chapter still apply in this case.

One can observe that, for low  $\omega_r$  speed rate, the lower sidebands have a high ripple already for low eccentricity values. Thus, this marks the lower sidebands dependency on the load.

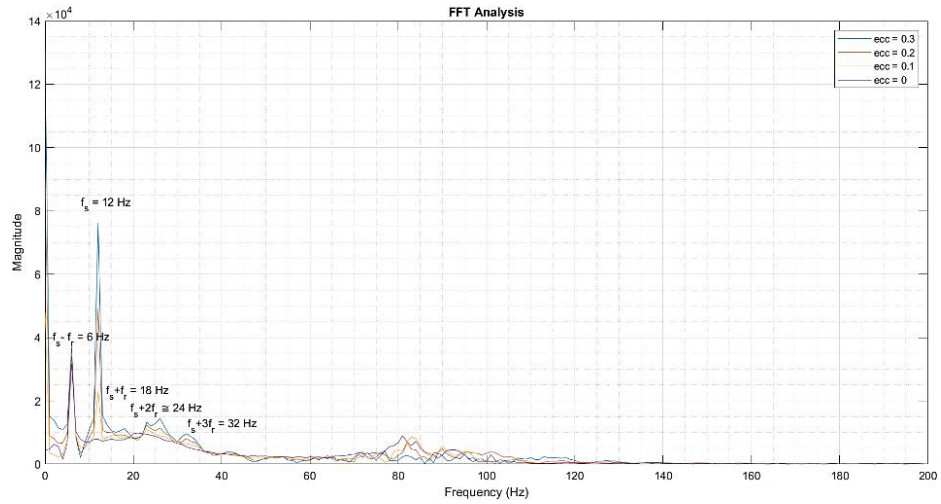


**Fig. 45** – FFT response of the current signal at  $0.3\omega_r$  with  $F = 200$  N.

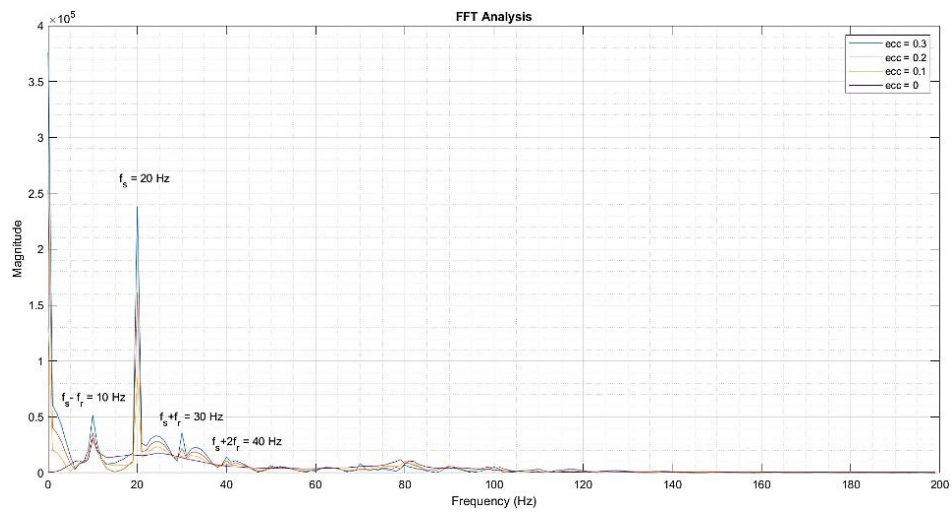


**Fig. 46** – FFT response of the current signal at  $0.5\omega_r$  with  $F = 200$  N.

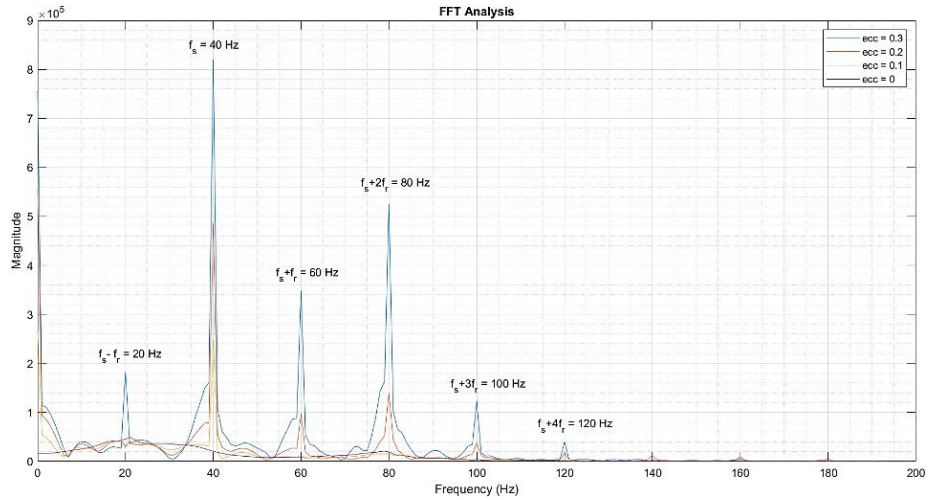


Fig. 47 – FFT response of the current signal at  $\omega_r$  with  $F = 200$  N.

### 8.2.2 Diagnosis with $F = 500$ N

Figures 48, 49, 50 show the phase current frequency spectrum for motor with increasing static eccentricity ratio with an external load equal to  $F = 500$  N. The corresponding experimental results show that, also in this case, the amplitudes of the harmonic components  $f_s \pm kf_r$  increase due to the increase in the load. In this condition, it was found that the maximum peaks magnitude for all the speed rates considered.

Here, as already done in the previous chapter, one can make the same considerations on the lower sidebands ripples.

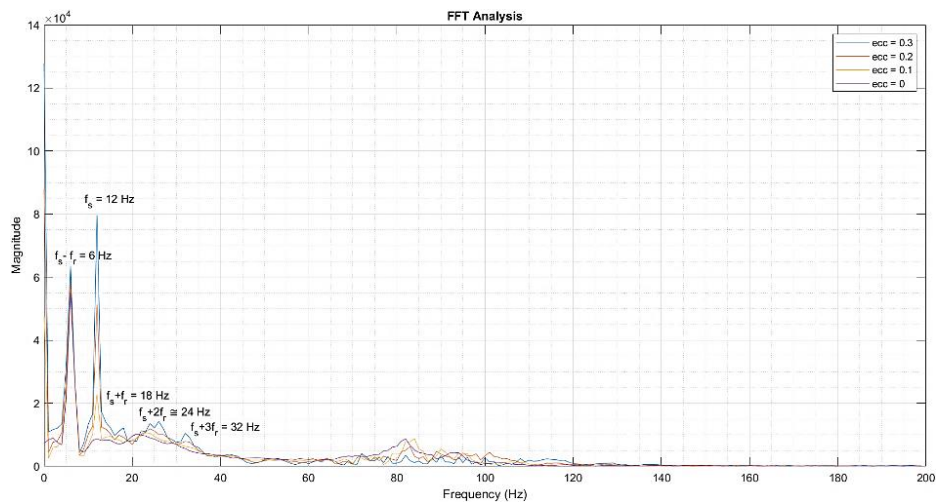


Fig. 48 – FFT response of the current signal at  $0.3\omega_r$  with  $F = 500$  N.

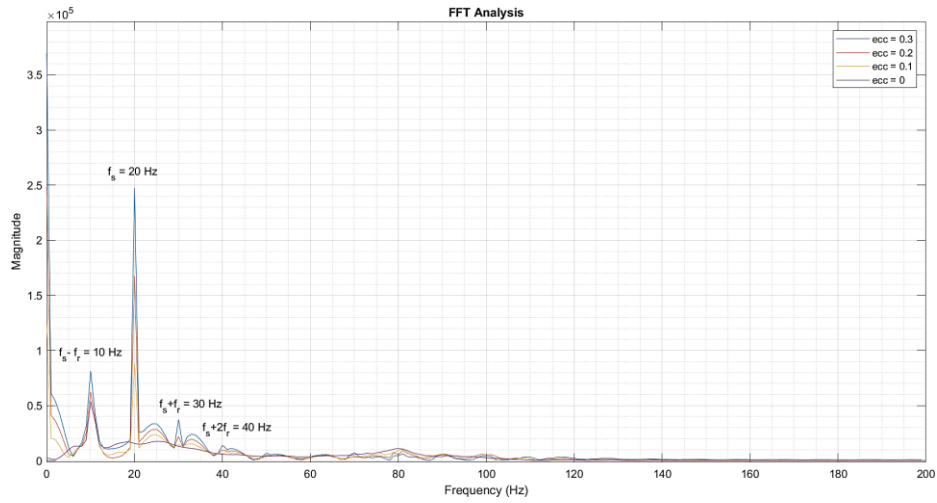


Fig. 49 – FFT response of the current signal at  $0.5\omega_r$  with  $F = 500 N$ .

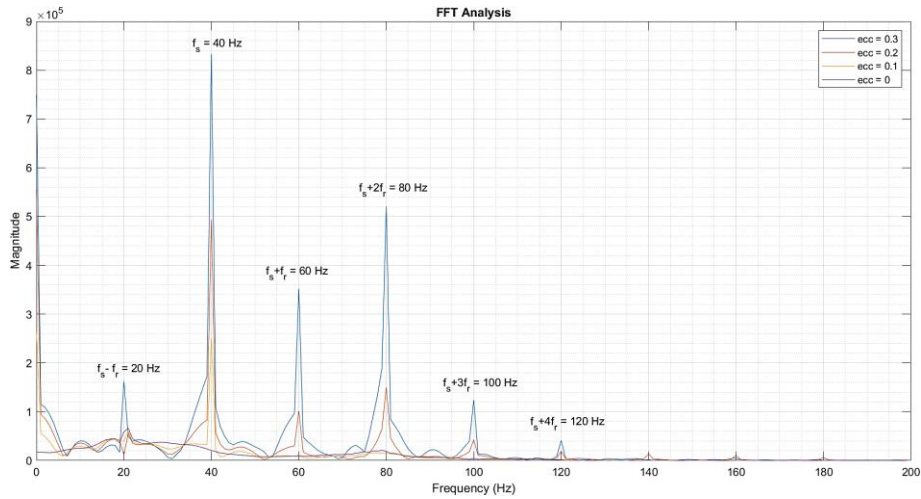


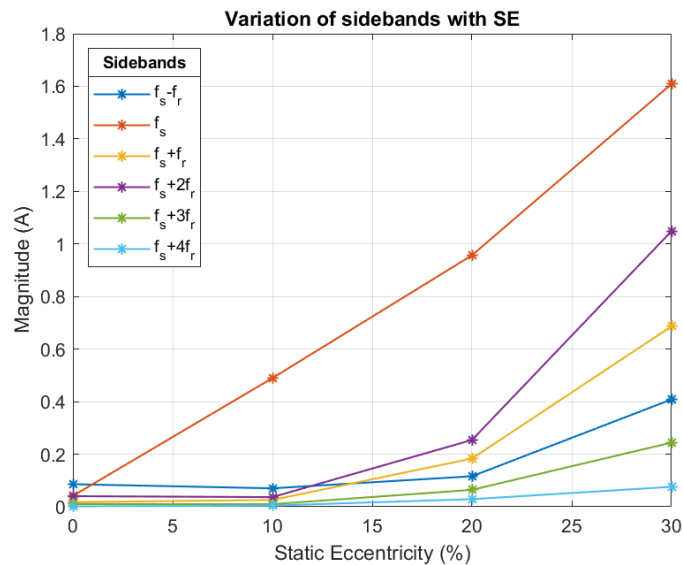
Fig. 50 – FFT response of the current signal at  $\omega_r$  with  $F = 500 N$ .

### 8.3 Result analysis

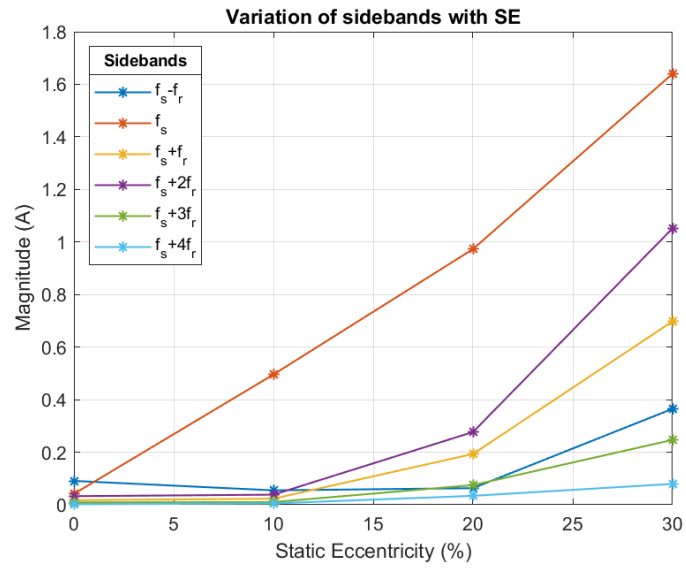
Sidebands frequencies of current signal  $i_a$  at  $f_s \pm kf_r$  were observed with zero levels of static eccentricity and increasing external load and rotor speed.

Figures 51, 52, 53 show that there is an increase in each sidebands peaks magnitude with the static eccentricity ratio, at the three different speeds for an increasing external load. It can be seen that the peaks increase from no-load to different load conditions, at different static eccentricity ratios. This raise involves all the sideband frequencies; however, this phenomenon is less regular for the upper and lower sidebands, except for the fundamental one  $f_s$ . In fact, the growth of  $f_s$  (shown in red) follows an upward increase that is almost linear, depending on the eccentricity ratio, as one can clearly see especially in Figure 48. Moreover, it is interesting that the lower sideband  $f_s - f_r$  (shown in blue) at reduced speed (Fig. 52 and 53) shows a rather flat trend, but it shifts towards higher values in function of increasing external loads. This indicates that, at lower speeds, since the external load affects the lower sidebands only, they can be used to detect and to monitor the presence of this type of disturb.

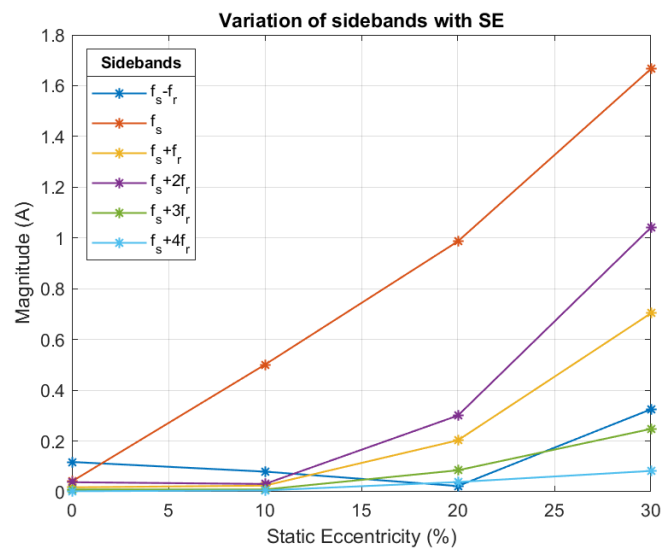
In view of these considerations, the FFT analysis is essentially an effective strategy to identify the amount of eccentricity affecting the system also in the presence of different types of disturbs, such as external load and rotor speed reduction.



(a)

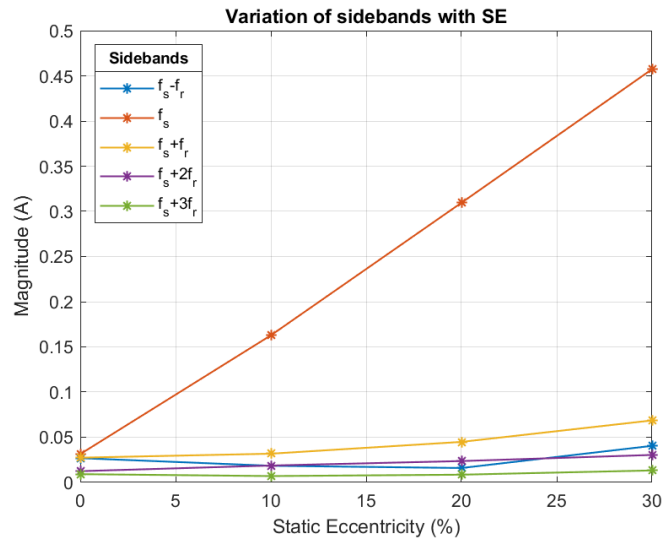


(b)

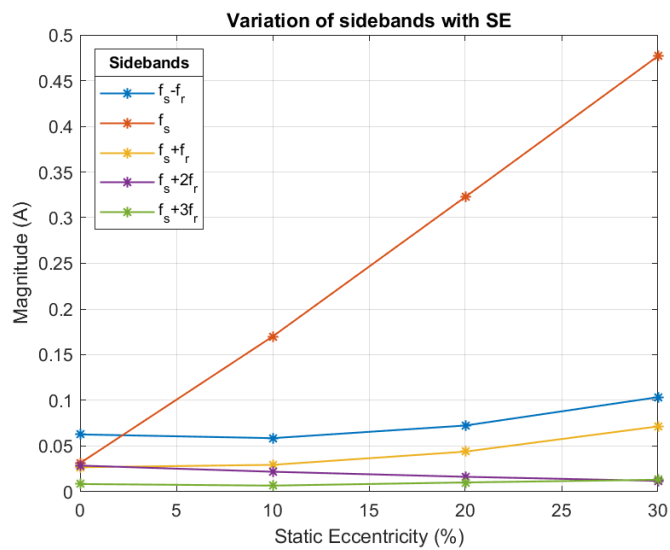


(c)

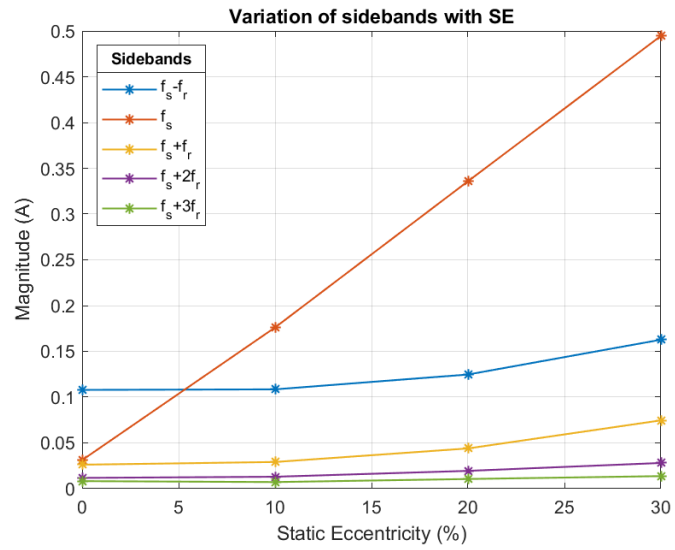
Fig. 51- Sidebands variation of current  $i_a$  with SE at  $\omega_r$ : (a) with no-load; (b) with  $F = 200N$ ; (c) with  $F = 500N$ .



(a)

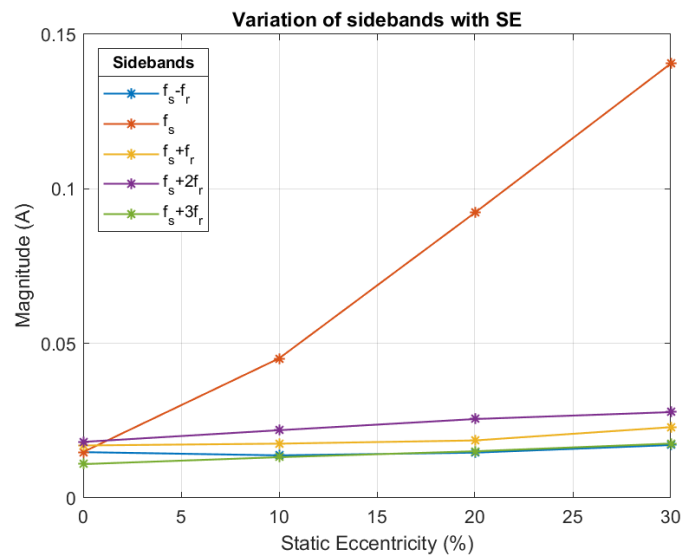


(b)

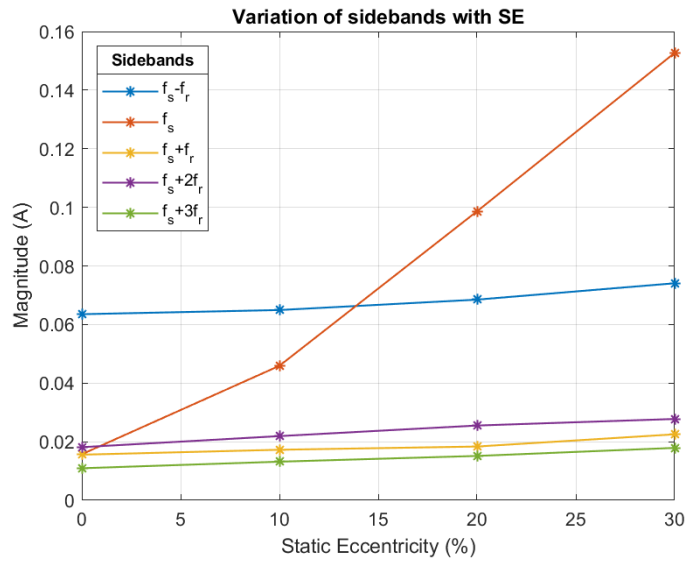


(c)

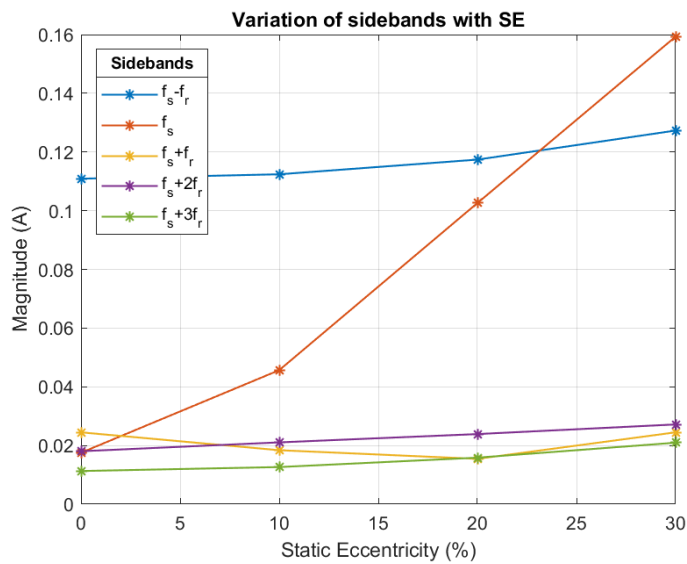
Fig. 52 - Sidebands variation of current  $i_a$  with SE at  $0.5\omega_r$ : (a) with no-load; (b) with  $F = 200N$ ; (c) with  $F = 500N$ .



(a)



(b)



(c)

**Fig. 53** - Sidebands variation of current  $i_a$  with SE at  $0.3\omega_r$ : (a) with no-load; (b) with  $F = 200N$ ; (c) with  $F = 500N$ .

## 8.4 Feature Extraction

The previous simulation investigations confirmed the linear dependency between the current frequency spectrum and the static eccentricity ratio. In fact, it can be seen that there is a presence of sideband frequencies inside the current frequency spectrum, as well as an increase of their peak magnitudes almost linear with the fault. Among all the peaks, the fundamental frequency peak is the one that shows an almost perfect linear dependency on the static eccentricity ratio. Thus, it can be used as Condition Indicator (CI), i.e. as a system feature, which characterizes the static eccentricity fault mode. In other words, since the main effect of this fault is the progressive worsening of the current unbalance, and thus the appearance of the sideband frequencies, the values of the feature will be related to the maximum peak of the current spectrum obtained from the FFT analysis. Then, because the obtained results depend also on the command input given to the model, that is depends on the derivative of the rotor position, this CI will be normalized by the absolute value of the rotor speed  $\omega_r$ :

$$CI_{SE} = \frac{\max(\text{abs}(fft(i)))}{|\omega_r|}$$

It must be considered that, the obtained feature should be normalized also by the external load value, which corresponds to normalize by the line current of the motor, even if in the reality there is an absence of reliable information on the aerodynamic load.

A significant step in the development of robust and accurate PHM algorithms, following the extraction and selection of the appropriate features or condition indicators CIs from raw data, is to verify their reliability and to delineate a fault grown model, but this is not addressed to this work.

# Chapter IX

## Conclusions and Further Studies

This Thesis aimed to verify the efficiency of the PHM methodology applied to a linear electromechanical actuator with a PMSM motor in the presence of one of the recurrent faults of this type of system, which is the rotor static eccentricity.

A deep study of the model was done in order to understand the best way to recreate the fault inside the considered system. An initial comparison between the healthy system and the eccentric one was taken to ensure that the system response would actually show a faulty behaviour.

After highlighting the most critical parameters of the system, the current response was chosen as the main indicator of the fault occurrence. In fact, thanks to the FFT analysis, it was possible to show that the current frequency spectrum, which is a function of rotor static eccentricity, presented some characteristic sidebands around the fundamental frequency demonstrating the presence of the fault, as predicted by most of scientific papers. This confirmed that FFT analysis is a powerful method for systems diagnosis; therefore, it can be used as a reliable starting point for the PHM analysis.

According to these investigations, it is possible to extract an index based on the current FFT analysis, which could show the presence of the rotor static eccentricity fault, in order to predict the fault occurrence and to proceed promptly with the maintenance of the system.

This Thesis only analyses the first step of the PHM framework, i.e. it performs the fault detection and, thus, its isolation and identification from a diagnostic point of view. The outcome agrees with what is found in literature and therefore merits further research. In this regard, a wider simulation set should be applied to the proposed model, in order to ensure the possibility to generalize the statements made, as well as the efficiency of the

## Conclusions and Further Studies

---

extracted feature for identification/diagnostic purposes. In fact, this work focuses on a restricted range of degradation phenomena, namely the static eccentricity, compared to all possible fault combinations due to several causes.

The obtained results encourage the extension of the proposed technique also to prognostic purposes, to probe the reliability of the fault index based on the current frequency spectrum.

A further step could be to verify if the reconfiguration control technique based on the MPC controller proposed in Chapter III improves the RUL of the system. For this purpose, after extracting the fault index, one must estimate a fault growth model, which represents the remaining life of the system. Since the MPC controller takes advantage of the relationship between the fault index and the RUL, it places more emphasis on reducing the magnitude of the index based on the RUL requirement. Hence, the MPC controller could be an interesting baseline for further study in the prognostics framework.

# Appendix

## A - Total Inertial Model on the Motor Shaft

The considered electromechanical actuator has a parallel interface between motor shaft and the screw-nut system. This means that, in order to realistically model the system, the inertia of all the different elements must be considered with respect to the same reference, that is, the motor shaft. The total inertia so obtained allows to compute the rotation equilibrium equation of the whole system [7].

In order to obtain the total inertia, the following expressions are considered:

- 1<sup>st</sup> axis inertia:  $J_1 = J_p + J_m$

- 2<sup>nd</sup> axis inertia:  $J_2 = J_p + J_{rs}$

- Transmission ratio of the SKF rollers-screw:  $\tau_{rs} = \frac{z}{2\pi} = \frac{x}{\theta_2} = \frac{\dot{x}}{\dot{\theta}_2} = \frac{\ddot{x}}{\ddot{\theta}_2}$

- Transmission ratio of the planetary reduction gearbox:  $\tau_g = \frac{\theta_2}{\theta_1}$

- Efficiency coefficient of the gearbox:  $\eta_g = \frac{T_2\theta_2}{T_1\theta_1}$

where  $J_p[kgm^2]$  is the pulley inertia,  $J_m[kgm^2]$  is the motor inertia,  $J_{rs}[kgm^2]$  is the SKF rollers-screw inertia,  $z$  is the number of the pole pairs,  $T_1$  and  $T_2 [Nm]$  are respectively the resistant torques applied by the first and by the second pulley.

Considering the equilibrium equations of the two axes and substituting the previous relationships, the following equations are obtained:

$$T_m - T_1 = J_1\ddot{\theta}_1$$

$$T_2 - T_3 = J_2\ddot{\theta}_2$$

where  $T_3 [Nm]$  is the torque acting on the rollers-screw coming from:

$$T_3 = \frac{x}{\theta_2} \frac{1}{\eta_{rs}} F = \frac{\tau_{rs}}{\eta_{rs}} F$$

with  $F = F_{ext} + m\ddot{x}$  and  $\eta_{rs}$  is the rollers-screw efficiency.

Therefore:

$$\begin{aligned} T_2 &= J_2 \ddot{\theta}_2 + \frac{\tau_{rs}}{\eta_{rs}} F = J_2 \ddot{\theta}_2 + \frac{\tau_{rs}}{\eta_{rs}} (F_{ext} + m\ddot{x}) = \frac{\tau_{rs}}{\eta_{rs}} F_{ext} + \ddot{\theta}_2 \left( J_2 + \frac{\ddot{x}}{\ddot{\theta}_2} \frac{\tau_{rs}}{\eta_{rs}} m \right) \\ &= \frac{\tau_{rs}}{\eta_{rs}} F_{ext} + \ddot{\theta}_2 \left( J_2 + \frac{\tau_{rs}^2}{\eta_{rs}} m \right) \end{aligned}$$

$$\begin{aligned} T_m &= T_1 + J_1 \ddot{\theta}_1 = \frac{\tau_{rs}}{\eta_{rs}} \frac{\tau_g}{\eta_g} F_{ext} + \ddot{\theta}_2 \left( J_2 \frac{\tau_g}{\eta_g} + \frac{\tau_{rs}^2}{\eta_{rs}} \frac{\tau_g}{\eta_g} m \right) + J_1 \ddot{\theta}_1 \\ &= \frac{\tau_{rs}}{\eta_{rs}} \frac{\tau_g}{\eta_g} F_{ext} + \ddot{\theta}_1 \left( J_1 + J_2 \frac{\tau_g^2}{\eta_g} + \frac{\tau_{rs}^2}{\eta_{rs}} \frac{\tau_g^2}{\eta_g} m \right) \end{aligned}$$

where the total inertia of the system is:

$$J = \left( J_1 + J_2 \frac{\tau_g^2}{\eta_g} + \frac{\tau_{rs}^2}{\eta_{rs}} \frac{\tau_g^2}{\eta_g} m \right)$$

## B - Sideband Frequencies Peaks Magnitude

**Tab. 5** – Magnitude [A] of sideband components at  $0.3\omega_r$  with  $F_{ext} = 0 N$ .

$F_{ext} = 0 N$						
SE (%)	$f_s - f_r$	$f_s$	$f_s + f_r$	$f_s + 2f_r$	$f_s + 3f_r$	$f_s + 4f_r$
<b>0</b>	0.01482	0.01458	0.01697	0.01813	0.01094	-
<b>10</b>	0.01377	0.04514	0.01756	0.02191	0.01318	-
<b>20</b>	0.01465	0.09227	0.0186	0.02552	0.0151	-
<b>30</b>	0.01711	0.1405	0.02288	0.02776	0.01789	-

**Tab. 6** - Magnitude [A] of sideband components at  $0.5\omega_r$  with  $F_{ext} = 0 N$ .

$F_{ext} = 0 N$						
SE (%)	$f_s - f_r$	$f_s$	$f_s + f_r$	$f_s + 2f_r$	$f_s + 3f_r$	$f_s + 4f_r$
<b>0</b>	0.02688	0.0314	0.02738	0.01247	0.00916	-
<b>10</b>	0.01843	0.1628	0.03179	0.01869	0.00704	-
<b>20</b>	0.01594	0.3095	0.04485	0.02365	0.00857	-
<b>30</b>	0.04046	0.4573	0.06862	0.3041	0.01325	-

**Tab. 7** – Magnitude [A] of sideband components at nominal speed  $\omega_r$  with  $F_{ext} = 0 N$ .

$F_{ext} = 0 N$						
SE (%)	$f_s - f_r$	$f_s$	$f_s + f_r$	$f_s + 2f_r$	$f_s + 3f_r$	$f_s + 4f_r$
<b>0</b>	0.08581	0.04155	0.01758	0.04031	0.01036	0.00167
<b>10</b>	0.07022	0.4897	0.02059	0.0367	0.00988	0.00459

## Appendix

<b>20</b>	0.1161	0.9571	0.1835	0.2541	0.06434	0.02894
<b>30</b>	0.4085	1.609	0.6867	1.049	0.2441	0.07586

**Tab. 8** – Magnitude [A] of sideband components at  $0.3\omega_r$  with  $F_{ext} = 200 N$ .

<b><math>F_{ext} = 200 N</math></b>						
<b>SE (%)</b>	<b><math>f_s - f_r</math></b>	<b><math>f_s</math></b>	<b><math>f_s + f_r</math></b>	<b><math>f_s + 2f_r</math></b>	<b><math>f_s + 3f_r</math></b>	<b><math>f_s + 4f_r</math></b>
<b>0</b>	0.06352	0.01572	0.01557	0.01813	0.01094	-
<b>10</b>	0.06494	0.09864	0.01725	0.02191	0.01318	-
<b>20</b>	0.06849	0.04591	0.01835	0.02552	0.01514	-
<b>30</b>	0.07408	0.1527	0.02252	0.02776	0.01789	-

**Tab. 9** – Magnitude [A] of sideband components at  $0.5\omega_r$  with  $F_{ext} = 200 N$ .

<b><math>F_{ext} = 200 N</math></b>						
<b>SE (%)</b>	<b><math>f_s - f_r</math></b>	<b><math>f_s</math></b>	<b><math>f_s + f_r</math></b>	<b><math>f_s + 2f_r</math></b>	<b><math>f_s + 3f_r</math></b>	<b><math>f_s + 4f_r</math></b>
<b>0</b>	0.06277	0.03135	0.02685	0.02868	0.00849	-
<b>10</b>	0.05869	0.17	0.02949	0.02193	0.00676	-
<b>20</b>	0.0725	0.3227	0.04394	0.0164	0.01023	-
<b>30</b>	0.1035	0.4768	0.07152	0.01195	0.01317	-

**Tab. 11** – Magnitude [A] of sideband components at nominal speed  $\omega_r$  with  $F_{ext} = 200 N$ .

<b><math>F_{ext} = 200 N</math></b>						
<b>SE (%)</b>	<b><math>f_s - f_r</math></b>	<b><math>f_s</math></b>	<b><math>f_s + f_r</math></b>	<b><math>f_s + 2f_r</math></b>	<b><math>f_s + 3f_r</math></b>	<b><math>f_s + 4f_r</math></b>
<b>0</b>	0.09071	0.04146	0.01737	0.03271	0.00893	0.00206

## Appendix

<b>10</b>	0.05485	0.4957	0.02304	0.03841	0.0102	0.00516
<b>20</b>	0.06314	0.9729	0.1933	0.2767	0.07489	0.03399
<b>30</b>	0.3651	1.64	0.6979	1.052	0.2469	0.07941

**Tab. 12** – Magnitude [A] of sideband components at  $0.3\omega_r$  with  $F_{ext} = 500 N$ .

<b><math>F_{ext} = 500 N</math></b>						
<b>SE (%)</b>	<b><math>f_s - f_r</math></b>	<b><math>f_s</math></b>	<b><math>f_s + f_r</math></b>	<b><math>f_s + 2f_r</math></b>	<b><math>f_s + 3f_r</math></b>	<b><math>f_s + 4f_r</math></b>
<b>0</b>	0.1109	0.01753	0.02448	0.01804	0.0113	-
<b>10</b>	0.1124	0.04567	0.01839	0.02106	0.01265	-
<b>20</b>	0.1174	0.1026	0.01545	0.02386	0.01585	-
<b>30</b>	0.1273	0.1593	0.02448	0.02717	0.2095	-

**Tab. 13** – Magnitude [A] of sideband components at  $0.5\omega_r$  with  $F_{ext} = 500 N$ .

<b><math>F_{ext} = 500 N</math></b>						
<b>SE (%)</b>	<b><math>f_s - f_r</math></b>	<b><math>f_s</math></b>	<b><math>f_s + f_r</math></b>	<b><math>f_s + 2f_r</math></b>	<b><math>f_s + 3f_r</math></b>	<b><math>f_s + 4f_r</math></b>
<b>0</b>	0.1079	0.03124	0.0262	0.01178	0.00826	-
<b>10</b>	0.1058	0.1761	0.02915	0.01304	0.00723	-
<b>20</b>	0.1247	0.3358	0.04395	0.01946	0.1056	-
<b>30</b>	0.1627	0.4946	0.07461	0.02809	0.01372	-

**Tab. 14** – Magnitude [A] of sideband components at nominal speed  $\omega_r$  with  $F_{ext} = 500 N$ .

<b><math>F_{ext} = 500 N</math></b>						
<b>SE (%)</b>	<b><math>f_s - f_r</math></b>	<b><math>f_s</math></b>	<b><math>f_s + f_r</math></b>	<b><math>f_s + 2f_r</math></b>	<b><math>f_s + 3f_r</math></b>	<b><math>f_s + 4f_r</math></b>
<b>0</b>	0.1175	0.04086	0.01758	0.0377	0.00902	0.00237

## Appendix

---

<b>10</b>	0.0794	0.5008	0.02427	0.03076	0.00900	0.00540
<b>20</b>	0.02258	0.9868	0.2028	0.3003	0.08467	0.03839
<b>30</b>	0.3249	1.666	0.7034	1.041	0.2476	0.08211

# Bibliography

- [1] G. Vachtsevanos, F. Lewis, M. Roemer A. Hess and B. Wu “Intelligent Fault Diagnosis and Prognosis for Engineering Systems.”, 2006, John Wiley & Sons, Inc. ISBN: 978-0-471-72999-0.
- [2] D. Brown, G. Georgoulas, B. Bole, H. Pei, M. Orchard, L. Tang, B. Saha, A. Saxena, K. Goebel, and G. Vachtsevanos. "Prognostics enhanced reconfigurable control of electro-mechanical actuators." In Annual conference of the prognostics and health management society, pp. 1-17. Rochester, NY: PHM Society, 2009.
- [3] Camacho E.F. & Bordons C., 1999. “Model Predictive Control”, Great Britain, Springer-Verlag London Limited.
- [4] The MathWorks, Inc, 2020, “Model Predictive Control Toolbox™ User's Guide (Release 2020a)”, retrieved on June 19, 2020 from [https://it.mathworks.com/help/pdf\\_doc/mpc/mpc\\_ug.pdf](https://it.mathworks.com/help/pdf_doc/mpc/mpc_ug.pdf) .
- [5] P. Giangrande, V. Madonna, G. Sala, A. Kladas, C. Gerada, M. Galea, “Design and Testing of PMSM for Aerospace EMA Applications”, IECON 2018 - 44th Annual Conference of the IEEE Industrial Electronics Society, Washington DC, USA, December 2018.
- [6] F. Jian, J. C. Marè, F. Yongling, “Modelling and simulation of flight control electromechanical actuators with special focus on model architecting, multidisciplinary effects and power flows.”, Chinese Journal of Aeronautics, 2017, 30(1): 47–65.
- [7] N. Ambrosino, “Implementazione di un servoattuatore elettromeccanico lineare a rulli planetari: progettazione dei software, modellazione e verifiche sperimentali.”, Tesi di Laurea Magistrale, Torino, relatore Prof. M. Sorli.

## Bibliography

---

- [8] J.R. Cameron, W.T. Thomson, A.B. Dow, 1986, “Vibration and current monitoring for detecting airgap eccentricity in large induction motors.”, IEE Proceedings, Vol. 133, Pt. B, No. 3, May 1986.
- [9] L. Frosini, “Analisi delle vibrazioni per la diagnostica delle macchine rotanti- II parte”, Dipartimento di Ingegneria Industriale e dell’Informazione Università di Pavia, [http://www-3.unipv.it/dmae/diagnostica/materiale\\_didattico/Diagnostica\\_2.pdf](http://www-3.unipv.it/dmae/diagnostica/materiale_didattico/Diagnostica_2.pdf), visited in 27/06/2020.
- [10] D.G. Dorrell, W.T. Thomson, S. Roach, “Analysis of airgap flux, current and vibration signal as a function of the combination of static and dynamic airgap eccentricity in three-phase induction motors.”, IEEE Transactions on industry applications, Vol. 33, No. 1, January/February 1997.
- [11] Z. Q. Zhu, Fellow, IEEE, L. J. Wu, and M. L. Mohd Jamil, “Distortion of Back-EMF and Torque of PM Brushless Machines Due to Eccentricity”, IEEE TRANSACTIONS ON MAGNETICS, VOL. 49, NO. 8, AUGUST 2013.
- [12] Nandi S., Toliyat H.A.& Li X. (2005) “Condition monitoring and fault diagnosis of electrical motors – a review.”, IEEE Transactions on Energy Conversion, Vol. 20, No.4.
- [13] Gokdere L.U., Bogdanov A., Chiu S. L., Keller K. J. & Vian J. (2006) “Adaptive control of actuator lifetime.”, IEEE Aerospace Conference, March 4-11.
- [14] A. De Martin, G. Jacazio, and G. Vachtsevanos, “Anomaly Detection and Prognosis for Primary Flight Control EMAs”, European Conference of The Prognostic and Health Management Society, 2016, p.7.
- [15] P.C. Berri, M. D.L. Dalla Vedova, P. Maggiore, F. Viglione, “A simplified monitoring model for PMSM servo-actuator prognostics”, MATEC Web of Conferences 304, 04013, EASN, 2019.
- [16] EM Weg Group, “The ABC’s of Synchronous Motors”, 09 December 2019, <https://static.weg.net/medias/downloadcenter/hfe/hf4/WEG-the-abcs-of-synchronous-motors-usaem200syn42-brochure-english.pdf>.

## Bibliography

---

- [17] M. Sundaram, "Implementing field-oriented control of a brushless DC motor", 01 April 2012, [www.eetimes.com/document.asp?doc\\_id=1279321](http://www.eetimes.com/document.asp?doc_id=1279321).
- [18] Encoders and Resolvers: [www.automationprimer.com/2012/07/15/encoders-and-resolvers](http://www.automationprimer.com/2012/07/15/encoders-and-resolvers), visited in 27/06/2020.
- [19] E.Elbouchikha, V.Choqueuseb, M.Benbouzid, "Induction machine bearing faults detection based on a multi-dimensional MUSIC algorithm and maximum likelihood estimation, ISA Transaction, Volume 63, July 2016, Pages 413-424.
- [20] D. Belmonte, M.D.L. Dalla Vedova, C. Ferro and P. Maggiore, (2017) "Electromechanical Actuators Affected by Multiple Failures: Prognostic Method based on Spectral Analysis Techniques.", AIP Conference Proceedings, June 2017.
- [21] Ahamed S., K., Sarkar A., Mitra M., Sengupta S.," NOVEL Approach for Detection of Inter-Turn Short Circuit of Induction Motor's Stator Winding through Envelope Analysis", 8th International Conference on Electrical and Computer Engineering 20-22 DECEMBER 2014, Dhaka, Bangladesh.